NUMERICAL AND EXPERIMENTAL INVESTIGATIONS OF AN AIR-COOLED BATTERY THERMAL MANAGEMENT SYSTEM

A Thesis Submitted to
The Graduate School of Engineering and Sciences of
Izmir Institute of Technology
In Partial Fulfillment of the Requirements for Degree of

MASTER OF SCIENCE

in Mechanical Engineering

by
Sinan GÖÇMEN

December 2021
İZMİR

ACKNOWLEDGMENTS

First of all, I would like to tell my deepest appreciation and give sincere thanks to my advisor Prof. Erdal ÇETKİN, for his continuous support and guidance during my studies and research.

I would like to thank my colleagues for their support and contributions. I would like to thank Turgay COŞKUN for his help and for sharing his experience with me. Also, I am thankful to Dr. Şahin GÜNGÖR as my project partner, for his support and contributions during this project.

We would like to thank The Scientific and Technological Research Council of Turkey (TUBITAK). This work is supported by TUBITAK under the grant number 218M498.

I would like to send my most sincere gratefulness to my beloved family, Kemal, Nurten, Safiye, and Deniz GÖÇMEN for their limitless support, encouragement, and love in every moment in my life.

Lastly, but most importantly, I would like to thank my fiancée, Tansu, for her endless love and support.

ABSTRACT

NUMERICAL AND EXPERIMENTAL INVESTIGATIONS OF AN AIR-COOLED BATTERY THERMAL MANAGEMENT SYSTEM

Electric vehicles play an integral role in eliminating pollution related to transportation, especially if electricity is generated via renewable sources. However, storing electricity onboard requires many battery cells. If the temperature of the cells is not strictly regulated, their capacity decreases in time, and they may burn or explode due to thermal runaway. Battery thermal management systems emerged for safe operations by keeping the battery cell temperatures under limit values. Here, we document that constant temperature distribution can be achieved with uniform coolant distribution to the channels located between batteries. To this end, we performed both numerical and experimental investigations. The design process of the developed battery pack begins with a design used in current packs. Later, how the shape of the distributor channel affects flow uniformity is documented. Then, the design complexity was increased to satisfy the flow uniformity condition, which is essential for temperature uniformity. The design was altered based on a constructal design methodology with an iterative exhaustive search approach. The uncovered constructal design yields a uniform coolant distribution with a maximum of 0.81% flow rate deviation along channels. The results also document that the peak temperature difference between the cells decreases from a maximum of 12 K to 0.4 K. Additionally, the developed design was simulated by using Newman, Tiedeman, Gu, and Kim (NTGK) electrochemical battery model, which provides more realistic results due to its heat generation approach in a battery cell. The accuracy of numerical studies is validated by experimental work.

Keywords: Battery Thermal Management, NTGK model, Temperature Uniformity, Forced Convection.

ÖZET

HAVA SOĞUTMALI BATARYA TERMAL YÖNETİM SİSTEMLERİNİN SAYISAL VE DENEYSEL İNCELENMESİ

Elektrikli araçlar, özellikle elektrik enerjisi yenilenebilir kaynaklardan elde ediliyorsa, ulaşım kaynaklı kirliliğin ortadan kaldırılmasında önemli rol oynamaktadır. Bununla birlikte, taşıt üzerinde elektrik enerjisinin depolanması için çok sayıda pil hücresi gerekir. Pil hücrelerinin sıcaklığı sıkı bir şekilde düzenlenmediği takdirde zamanla kapasiteleri düşer ve termal kaçak nedeniyle yanabilir veya patlayabilirler. Hücre sıcaklıklarının sınır sıcaklık aralığında tutarak güvenli operasyonlar için pil ısıl yönetim sistemleri ortaya çıkmıştır. Bu çalışma, pil hücrelerinin arasında bulunan kanallara soğutucu akışkanı homjen bir şekilde dağıtılmasıyla sabit sıcaklık dağılımının sağlanabileceğini belgelemektedir. Bu amaçla, hem sayısal hem de deneysel çalışmalar gerçekleştirilmiştir. Bu çalışmada geliştirilen pil paketinin tasarım süreci, mevcut paketlerde kullanılan bir tasarımla başlamaktadır. Daha sonra dağıtıcı kanalın şeklinin akış homojenliğini nasıl etkilediği araştırılmıştır. Ardından, sıcaklık homojenliği için gerekli olan akış homojenliği koşulunu sağlamak için tasarım karmaşıklığı artırıldı. Tasarım, kapsamlı bir iteratif araştırma yaklaşımıyla yapısal tasarım metodolojisine dayalı olarak değiştirildi. Ortaya çıkarılan tasarım, kanallar boyunca maksimum %0,81 hava debisi sapması ile homojen bir hava dağılımı sağlamaktadır. Geliştirilen tasarım basit ve konik manifold tasarımlarına göre üretimi oldukça kolaydır. Ayrıca, elde edilen sonuçlar, hücreler arasındaki maksimum sıcaklık farkının maksimum 12 K'den 0,4 K'e düştüğünü göstermektedir. Ek olarak, geliştirilen tasarım, sabit olmayan ısı üretimi yaklaşımına sahip Newman, Tiedeman, Gu ve Kim (NTGK) elektrokimyasal pil modeli kullanılarak simülasyonları gerçekleştirilmiştir. Elektrokimyasal model, batarya paketi seviyesinde aynı anda akış ve enerji sayısal çözümlemeleri yapılmıştır. Sayısal çalışmaların doğruluğu deneysel çalışmalarla doğrulanmıştır. Sonuçlar, sıcaklık farkında minimum sapma ile maksimum sıcaklığın istenen çalışma sıcaklığının altında tutulabileceğini göstermektedir.

Anahtar Kelimeler: Batarya Termal Yönetimi, NTGK model, Homojen Sıcaklık Dağılımı, Zorlanmış Taşınım.

TABLE OF CONTENTS

LIST OF FIGURES

Figure **Page**

Figure **Page**

LIST OF TABLE

LIST OF SYMBOLS

$\bar{P}$	Average pressure	Pa
Q_{nom}	Total electric capacity	Ah
Q_{ref}	Reference capacity	Ah
$\bar{T}$	Average temperature	K
T_{ref}	Reference temperature	K
c_p	Specific heat capacity	$J\ kg^{-1}\ K^{-1}$
$\dot{m}$	Mass flow rate	$kg\ s^{-1}$
$\dot{q}$	Heat generation rate	W
$\bar{u}$	Average velocity component in each direction	$m\ s^{-1}$
H_{in}	Height of inlet region	mm
H_{out}	Height of inlet region	mm
j_{ECh}	Volumetric current transfer rate	
j_{short}	Current transfer rate	
k	Turbulent kinetic energy	$m^2\ s^{-2}$
L_{in}	Length of the inlet region	mm
L_{out}	Length of the outlet region	mm
P	Pressure	Pa
t	Time	s
T	Temperature	K
u'	Fluctuations of velocity in each direction	$m\ s^{-1}$
u	Velocity vector	$m\ s^{-1}$
W_{in}	Width of the inlet region	mm
W_{out}	Width of the outlet region	mm
DoD	Depth of discharge	
Vol	Volume of the active zone	
x	Component of the energy dissipation rate	m

Greek letters

ΔT	Temperature difference	K
ε	Turbulent kinetic energy dissipation rate	$m^2\ s^{-3}$
μ	Viscosity	$Pa\ s$
ρ	Density	nm
σ_k	Turbulent Prandtl number for k	
σ_ε	Turbulent Prandtl number for ε	
σ_{cp}	Turbulent Prandtl number based on specific heat at constant pressure	
σ_+	Effective electric conductivity for the positive electrodes	
σ_-	Effective electric conductivity for the negative electrodes	
φ_+	Phase potential of positive electrodes	
φ_-	Phase potential of positive electrodes	
λ	Conductivity	$W\ m^{-2}\ K^{-1}$

CHAPTER 1

INTRODUCTION

The effect of climate change is becoming more pronounced due to natural disasters and droughts related to it. Air pollution and greenhouse gas emissions are responsible for global warming. Internal combustion engines also have a significant responsibility in environmental pollution and conduce to increase the use of renewable alternatives in industry and transportation[1]–[3]. During the Covid-19 pandemic, demand for transportation had significantly declined, which yielded the air quality increase in densely populated cities. Even before the pandemic, electrified technologies were financially and politically supported, and this changeover was getting mandatory according to the regulations on carbon emission. Therefore, many countries commit to reducing carbon emissions the mitigating their adverse effects[4]. Furthermore, International Energy Agency has recently reported that more than 20 countries restricted the sale of fossil fuel vehicles or required that all new sales zero-emission vehicles[5].

In the near future, the transition to electric vehicles (EVs) powered by renewable energy sources will play a vital role in achieving the aim of zero emission. In contrast to internal combustion engine vehicles, pure electric vehicles are more efficient and have a lower environmental impact, particularly when electricity is produced from renewable sources. The acceleration of this electrification process is also directly dependent on battery technologies. Currently, electric vehicles generally come with rechargeable lithium-ion (Li-ion) batteries that have advantages in comparison to competing batteries, such as greater energy density[6], specific power and recyclability, lighter weight[7], lower self-discharge rate[8], longer life cycle[9] and no memory effect[10]. However, there are also drawbacks such as range, charging time, capacity fade, and safety which are directly affected by environmental conditions and operating temperature[11]. Hence, the research and development studies are concentrated on improving the battery characteristics and the operating conditions[12]–[14]. Generated heat during charge/discharge and heating requirements for cold climates result in temperature variation in battery packs. Therefore, advanced thermal management systems with strict temperature control are required to keep the temperature in the desired range to eliminate

safety risks (thermal runaway) and capacity fade related to above the desired temperature range, especially in ultra-fast charging and discharging[15]–[18]. In addition, the temperature in modules should be uniform to prolong battery life and operate efficiently[19]. Temperatures out of the desired range can lead to capacity loss, power fade, and aging[20]. This situation can also cause serious accidents occurred in specific applications where LIBs are used[21]–[23]. Therefore, the effectiveness of thermal management systems (BTMSs) plays an integral role in providing desired performance and safety in LIB packs, and also literature documents numerous studies with the aim of designing a proper battery thermal management system via simulating electrochemical behavior of cells with the thermal characteristics of them.

Even though there are many publications on the thermal management of battery packs, the literature lacks in documenting how battery packs should be designed in order to distribute coolant/air effectively and control the battery cell temperature strictly. Rather, literature relies on improvements on manifold designs where random design parameters or port positions are analyzed. Here, we first document how all the battery cells can be kept under the desired temperature with the improved battery pack design for advanced electric vehicles by considering the constructal design approach. The constructal design takes a systematic approach to reduce resistances in a flow structure[24]. In this way, the developed design is aimed to distribute fluid evenly by achieving the same pressure drop along each flow path between battery cells. The uniform air distribution to each cell in a pack eliminates non-uniform temperature distributions of battery cells in packs. Secondly, the developed design was simulated by using Newman, Tiedeman, Gu, and Kim (NTGK) electrochemical battery model, which provides more realistic results due to its heat generation approach in a battery cell. The electrochemical model was simulated with fluid and heat flow simultaneously at the battery pack level. Lastly, we compared the numerical results with our experimental study.

The following alignments will be used to clarify the thesis's structure; in Chapter 2, the literature scientific state of the modeling of lithium-ion batteries as well as the existing thermal management systems will be reviewed. In chapter 3, the modeling of the cell will be demonstrated with the validation results and the methodology will be explained. Chapter 4 includes the experimental setup and procedures. The results of the developed and optimized thermal management design will be detailed in all numerical and experimental analyses with figures and tables in Chapter 5. Finally, in chapter 6, the conclusion will be clarified according to numerical and experimental results.

CHAPTER 2

LITERATURE REVIEW

First, the thermal characteristics of lithium-ion battery cells used in EV battery packs are discussed in this chapter. Then, the electrochemical-thermal models of the cells were examined to model more realistic cell behavior for thermal control. Finally, state of art of thermal management systems is reviewed considering all types of thermal control strategies.

Besides lead-acid[25]–[28], nickel-metal hydride and nickel-cadmium (NiCd) batteries are utilized in the EV and hybrid electric vehicle (HEV) sectors, most commonly, lithium-ion (Li-ion) batteries are used due to benefits such as high energy density, lightweight, and high recyclability[6], [7]. A Ragone plot illustrating the specific energy and power of battery cells for various application goals was given in Figure 2.1. As can be seen in the figure, LIBs significantly outperform compared to other cell chemistries in electric vehicles. Lithium-based battery cells show much better performance in terms of specific energy and energy density relative to the nearest competitive of nickel-metal hydride (Ni-MH) cells. Comparison of energy densities of Li-ion and Ni-MH cells states that LIBs have energy density characteristics which are more than 40%[29]. Therefore, li-ion batteries are seen as having the most promising cell chemistry for electric vehicles.

The major component of an electric vehicle is its battery pack, which has critical drawbacks such as cost, range, and safety apart from mentioned advantages. In order to overcome these obstacles, many studies on the electrode and electrolyte materials (active materials) of lithium-based batteries have been conducted in the literature. There are several Li-ion cell types with various characteristics. Generally, LIBs are named according to using active materials, which directly affect cell performance. A comparison of common LIBs used in EVs is shown in Figure 2.2.

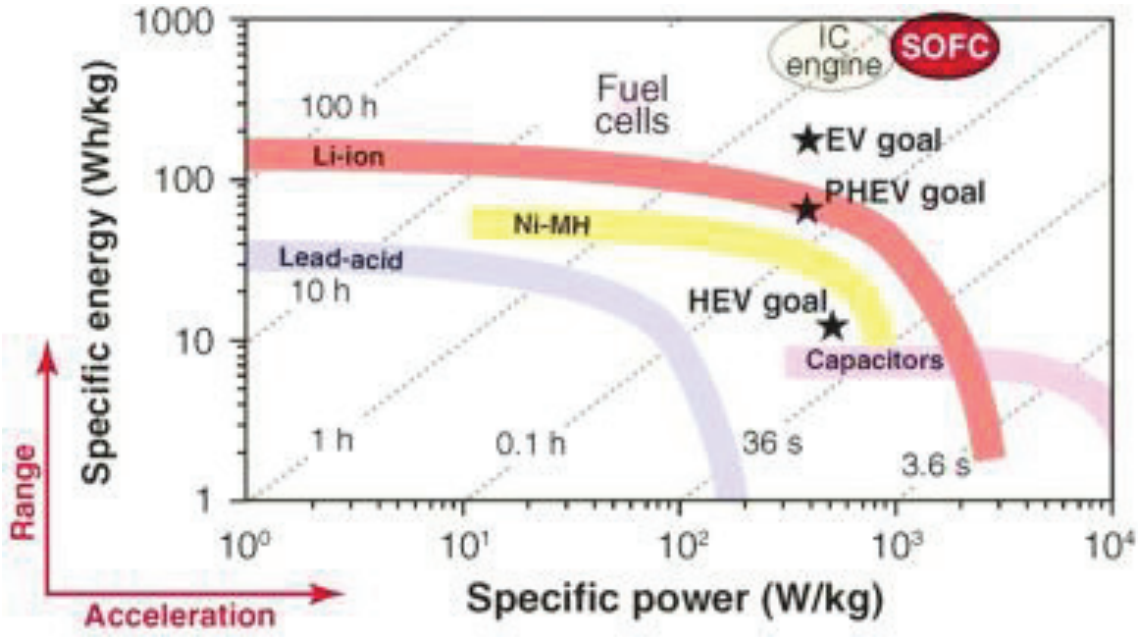

Figure 2.1. Ragone plot of different electrochemical energy storage and conversion devices [123]

In the figure, the size of the colored areas has a positive meaning in the graphics where the abbreviated form of the battery names determined according to the active material is given. Specific energy, specific power, cost, performance, safety, and life span have been identified as the main criteria for comparison. It is stated that Li_2TiO_3 (LTO) batteries are one of the cells with the best chemical structure in terms of safety, life span, and performance. However, there are some disadvantages such as low specific energy and high cost. On the other hand, $LiFePO_4$ (LFP) cells are one of the best options for electric vehicles due to their significant merits, such as low cost, low toxicity, high performance, and stability. In addition, LFP cells are known as having one of the safest cell chemistries. Therefore, LFP cells have been discussed in many studies. Lithium-ion batteries, however, are still confronted with various obstacles that adversely affect the mentioned merits as performance, safety, and life, etc. One of the main reasons for these barriers is temperature.

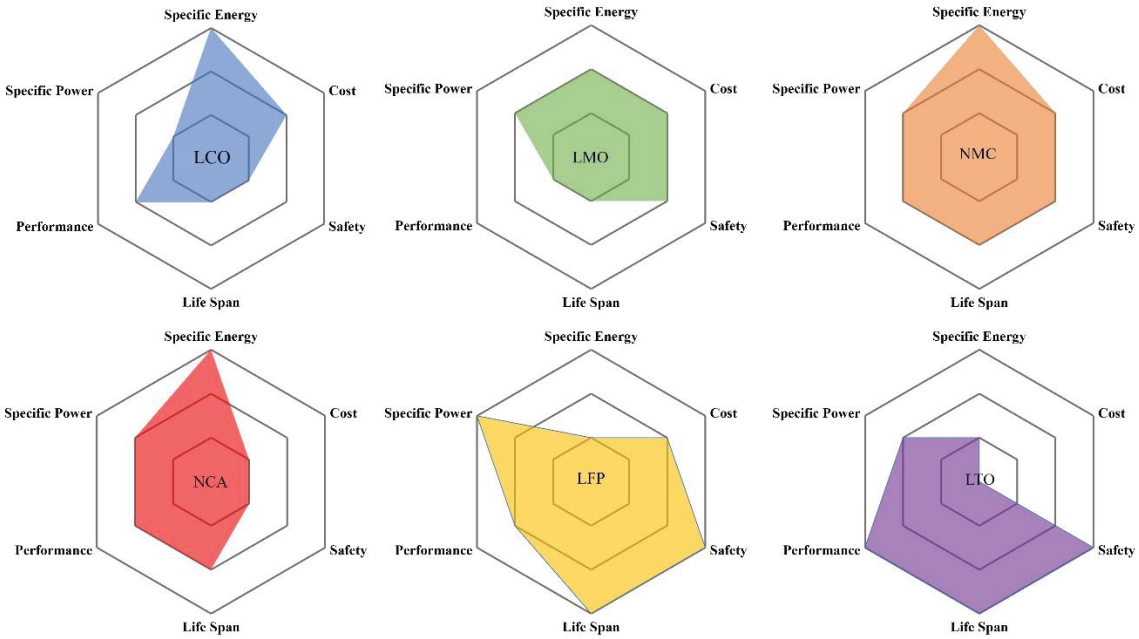

Figure 2.2. Comparison of various types of LIBs used in EVs [30].

The performance of lithium-ion batteries is significantly affected by the operating temperature. The lithium-ion batteries can be exposed power and capacity fade when the temperatures exceed 50°C. On the other hand, the low temperatures below -10°C can also cause reduced capacity and lithium plating[31]. Therefore, the thermal management strategies are essential, and a battery thermal management system should be carefully designed to keep Li-ion Battery (LIB)s between the optimal temperature range of 15°C – 35°C in spite of the LIBs have a large operating temperature range of -20°C – 60°C [32]. Additionally, the temperature difference among each battery cell and module should be minimized and be less than 5°C [33]. Thus, safety risks and aging of cells are eliminated; hence, the lifetime and performance of the batteries are increased. In addition to these temperature limitations, it is also very important to develop models that predict the heat generation and temperature distribution characteristics of batteries. Consequently, the literature documents numerous studies with the aim of designing a proper battery thermal management system via simulating the electrochemical behavior of cells with their thermal characteristics.

Experimentation and numerical simulations are the most prevalent ways of analyzing the effect of battery thermal behavior and thermal management. In general, thermal management systems are investigated using computational fluid dynamics (CFD) and finite element methods (FEM). There are many studies that were developed mathematical and numerical models for analyzing the thermal behaviors of batteries.

Doyle et al. modeled a galvanostatic charge and discharge of a lithium polymer cell using concentrated solution theory [34]. Chen and Evans developed two-dimensional and three-dimensional models to examine the behaviors of lithium polymer and lithium-ion batteries at various C-rates [35]–[37]. Wang et al. developed thermal and electrochemical models for LIBs, which are two-dimensional [38]. Kwon et al. examined the potential and current density distribution on the electrodes of a LIB with the model they had developed at 25°C ambient temperature [39]. Kim et al. also presented a two-dimensional thermal model to show the dependence of the discharge behavior of a LIB on the variation of ambient temperature [40].

In the last period, the literature focuses on various battery thermal management strategies, and many BTMS designs were developed by using only one strategy or hybridization of them. Generally, thermal management strategies are categorized as active and passive systems depending on their external energy requirement. Active systems require an external source for circulation of a working fluid to keep the batteries in the optimal temperature range, while the passive ones do not as they rely on latent heat requirement being comparatively great during phase change [41]–[46]. In addition, they are also divided into four sub-categories according to used heat transfer medium[17]: air[47]–[49], liquid[50]–[52], phase change material (PCM)[53]–[55] and combination of them. Each strategy has advantages and disadvantages based on its ease of use, cost, maintenance, life, and efficiency. For instance, air-based thermal management systems have been used due to the low cost and ease of adaptability in many energy storage applications [56]. However, there are some challenges to making them more efficient and compact because of the thermal properties of air (low thermal conductivity and specific heat), energy consumption for cooling, homogeneous distribution of air [57]–[60]. On the other hand, liquid-based strategies (mostly preferred by EV manufacturers) also have disadvantages such as complexity, cost, leakage, even though they are more efficient and compact than air-based systems [61]. PCM is another key element of thermal management strategies due to its high latent heat. Nowadays, PCM-based thermal management strategies are paid attention to due to their potential for their simplicity in application, low-cost, effective heat transfer [62]. However, low thermal conductivity, additional weight, and volume changing during phase change are seen as their drawbacks[63].

Air-cooled BTMSs are the most preferred single-phase cooling solution due to ease of integration with other methods and applications. Generally, the batteries are in

direct contact with air for cooling. The parallel cooling method is widely used to cool battery packs, including pouch or prismatic cells, compared to cylindrical cells, because of the complexity and difficult integration of plenums. Figure 2.3 shows the common manifold design in the field. The coolant is driven into the battery pack by fans and flow over the battery cells through the pack. Hence, heat is transferred from the cells to the working fluid. However, the homogeneous temperature distribution in the pack cannot be achieved until the optimum battery cell arrangement, and airflow configuration are uncovered. Varying flow rates, flow paths, positions of inlet/outlet sections of air, spacing between the batteries, and layout of the batteries are common investigation objectives to enhance heat transfer. [64]–[70]

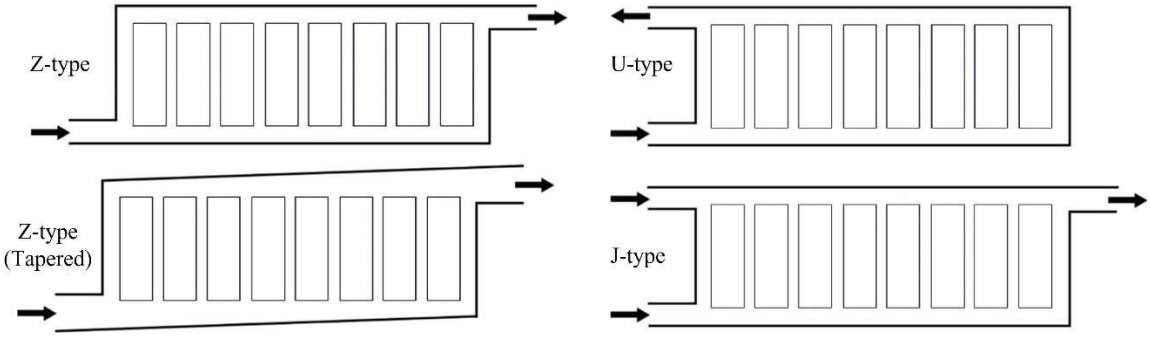

Figure 2.3. Schematic of common manifold designs using in BTMS.

Accordingly, there are numerous numerical and experimental studies on air-cooled BTMSs[71]–[77]. For instance, Chen et al.[71]–[73] documented the effect of spacing between the battery cells for several manifold models with air cooling. Their objective was to minimize the maximum temperature of the pack and cells and to obtain a more uniform temperature distribution within the battery pack. Park[74] analyzed the cooling performance of five manifold designs without changing the layout or design of the existing battery system. Xu and He[75] conducted numerical simulations for a variety of airflow duct configurations, including horizontal, longitudinal, and U-type models. The major goal of the study is to improve the heat dissipation performance of the pack design. In comparison to the horizontal battery pack design, the longitudinal battery pack design adheres to a more uniform temperature distribution. However, it does not meet the safety requirements; hence U-type was also considered. They suggested using a double U-type duct design for air-cooled battery packs as the first option. The thermal behavior of Li-ion pouch cells used in a hybrid electric vehicle was studied by Sun and Dixon [76]. The

effects of the cooling channel, duct, and corrugation on battery pack design were studied using the design of experiments. For a battery pack case with 80 Li-ion pouch cells, constant cross-sectional design inlet and outlet ducts were initially investigated. Temperature fluctuations of up to 10°C were reported for this system. They discovered that using a Z-type manifold reduces fluctuation and that using a Z-type manifold with conductive cooling plates is the optimum approach. Xie et al.[77] ptimized inlet angle and the gap between Li-ion batteries in a pack. Computational fluid dynamics (CFD) simulations were used to analyze the effects of battery pack manifold design, and the results were validated by experiment. They documented that the maximum temperature and the temperature difference become minimum when air inlet and air-outlet angles are 2.5°. Liu et al.[78] also presented a new "J-type" manifold design by merging "U-type" and "Z-type" designs. It is stated that the temperature uniformity can be improved by controlling the outlet valves according to heat load change at the different sides of the manifold. Cetkin[79] documented the effect of manifold design on the flow rate distribution in a microdevice. He documented how the manifold shape should be in order to distribute fluid evenly to channels. Labaek et. al. [80] documents pressure drop and air distribution of two distinct manifold models experimentally for fuel cell applications: U- and Z-type. They document the diffuser type connection enhances flow rate uniformity; however, the variation in flow rate distribution varies between 10-20% even for the improved design. Shadid and Chaab[81] numerically analyzed the thermal performance of various manifold models for pack designs with cylindrical Li-ion batteries. They showed that case B is the best design in terms of temperature uniformity where the maximum temperature in the pack can be reduced by 9%. Chen et al. [46] document the effect of air inlet and outlet port locations on maximum temperature and maximum cell temperature difference. The maximum temperature and maximum cell temperature difference were reduced by 4.5 K and 7.7 K with optimized air-cooled BTMS.

Varying flow rates, flow paths, positions of inlet/outlet sections of air, spacing between the batteries, and layout of the batteries are common investigation objectives to enhance heat transfer from the cells [45], [49], [66], [67], [69], [70], [82], [83]. Jiaqang et al. [84] investigated different air cooling strategies, including various air inlet and outlet configurations for a battery pack consisting of 60 cylindrical cells. The results show that the lateral located inlet and outlet regions at different sides perform more effectively than the same side configuration. Wang et al. [85] examined the thermal performance of battery modules with several fan locations and cylindrical battery cell arrays, including

1×24, 3×8, and 5×5 rectangle arrays, 19 cells hexagonal arrays, and 28 cells circular arrays. They uncovered that the cubic (5×5 rectangular) arrangement in Figure 2.4 (a) provides the best cooling capability when the fan is positioned at the top of the module. In addition, the hexagonal structure is described as the best option considering space utilization, as shown in Figure 2.4 (b). Yang et al. [86] conducted comparative analyses to investigate the effects of transverse and longitudinal spacing on the cooling performance for the staggered and aligned cylindrical battery cell layouts, as shown in Figures 2.4(c) and 2.4(d), respectively. The study shows that the temperature rise on the cells increases as longitudinal and transverse intervals increase for staggered arrays. However, optimization of the longitudinal spacing reduces temperature rise for aligned battery arrangement. They stated that the alignment arrangement should be selected with consideration of thermal management as it affects temperature uniformity significantly.

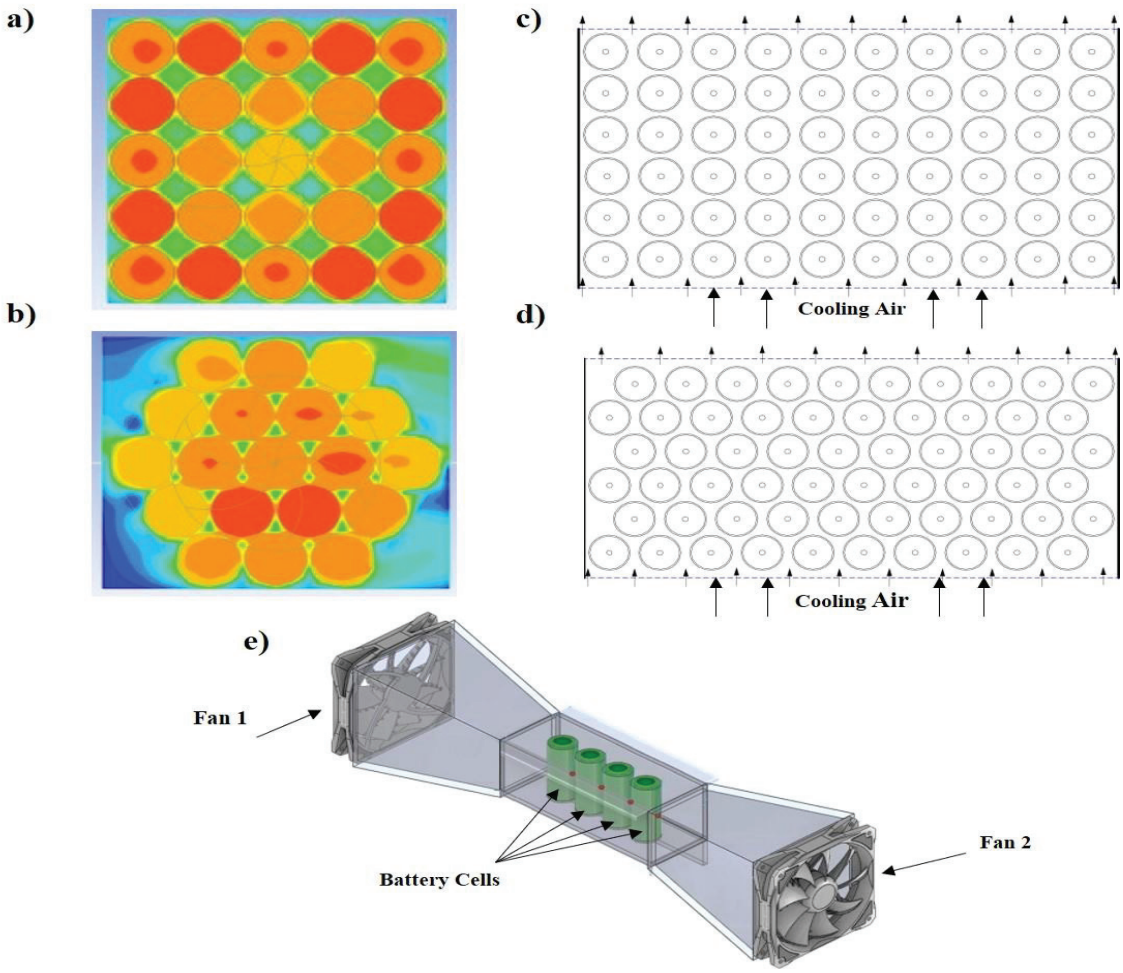

Figure 2.4. (a-b) The cubic and hexagonal structure when the fan is positioned at the top of the module [85], (c-d) the aligned and staggered cell layouts [86], (e) the battery module cooling with the active control using reciprocating airflow [87].

On the other hand, He et al. [87] studied battery module cooling with active thermal control using reciprocating airflow, which is generated by two fans placed at the inlet and outlet of the tunnel. In Figure 2.4(e), the cylindrical type 26650 LIB cells, which have the capacity of 2.6Ah, were aligned in a row in the tunnel, and only their lateral external surfaces are in contact with the airflow. The study shows that the case using active control and reciprocating flow reduces the parasitic power consumption up to 84%. However, the temperature rise on the cells slightly increases to 0.5°C compared to the case using no active control. Similarly, Mahamud et al. [88] performed two-dimensional CFD simulations in order to cool the battery pack, which has aligned cylindrical battery configuration using reciprocating airflow. They aimed to increase temperature uniformity with their cooling system that reverses the airflow periodically. The results show that the reciprocating airflow reduces the temperature difference between the battery cells by approximately 4°C and the maximum cell temperature by 1.5°C. Ozdemir et al. [89] documented experimental results of 18650 (3.25 Ah) cylindrical LIB under cycles with 0°C, 20°C, and 50°C operating conditions. Furthermore, the experimental results were compared with COMSOL lumped battery model results under 0.5C, 1C, and 1.5C discharge rates. Thermal results of the 2-dimensional axisymmetric lumped model are very close to the experimental ones. They have also documented that the internal resistance behavior was unstable, and they proposed that the battery cells should not be fully discharged to achieve more uniform internal resistance under operations.

Air-based BTMSs may remain incapable of providing adequate cooling for battery packs due to the low conductivity and heat capacity of air (low heat transfer coefficient compared to liquid-cooling with working fluids of water, water-glycol mixture, oil, or equivalent liquid mixture as coolant) when C-rate increases, battery pack consists of many cells, extreme environmental conditions, etc. However, liquid BTMSs have disadvantages such as complexity, cost, leakage potential, even if they are more efficient and compact than air-based systems. Liquid-based BTMSs have distinct strategies such as direct or indirect (submerging the batteries in a dielectric coolant fluid) cooling. Direct cooling can be considered as much better than indirect cooling in terms of high heat transfer rate, simplicity, packaging density, and cost. However, direct cooling of the batteries has several drawbacks such as electrical short, corrosion, and increase in weight as all the systems are submerged in liquid. Moreover, it is not usually preferred in electric vehicle applications from the practical aspects of systems [90]. Nevertheless, the

strategy has been used in other application areas for battery thermal management [91]–[95].

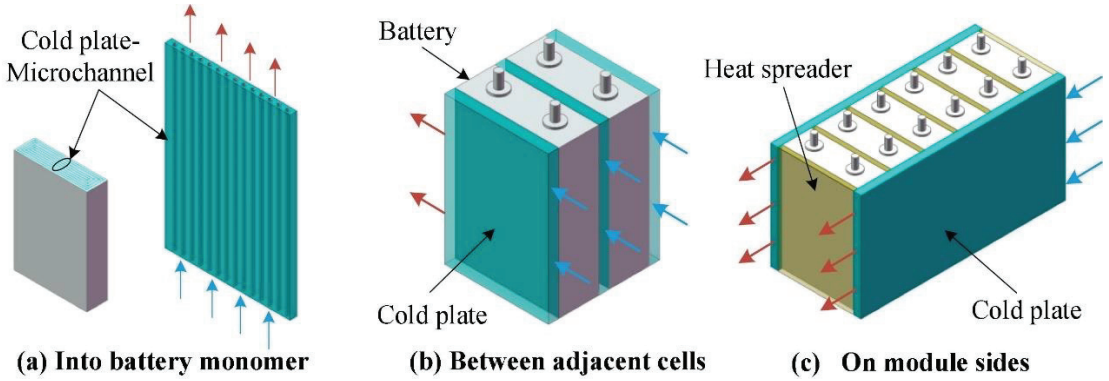

Figure 2.5. Configurations of cold plates with different locations [96]

On the other hand, indirect cooling is commonly used with cold plates with integrated channels and fins, sandwiched or side attaching structure (Fig. 2.5) and preferred by the electric vehicle manufacturers (such as Tesla, Chevrolet, GM, etc.), although the thermal resistance which occurs in indirect cooling strategy reduces the heat transfer rate compared to the direct liquid cooling. Liquid cold plate cooling is the most preferred option in battery packs, including pouch and prismatic cells. This becomes more difficult to apply in cylindrical cells due to inconsistency between cell geometry. The indirect cooling strategy is distinguished as a suitable method for most practical applications [58]. EV manufacturer Tesla developed a curvy channel structure (Figure 2.6(a)) around the cylindrical battery stacks to cool the battery pack of Model S [97], [98]. The water-glycol mixture runs as the coolant in the curvy channels, which have a radius of nearly equivalent to the outside radius of cells. The coolant contacts partially and passes through the cells as a series. This situation seems not much efficient. However, it is a good solution in terms of safety, manufacturability, and practicality.

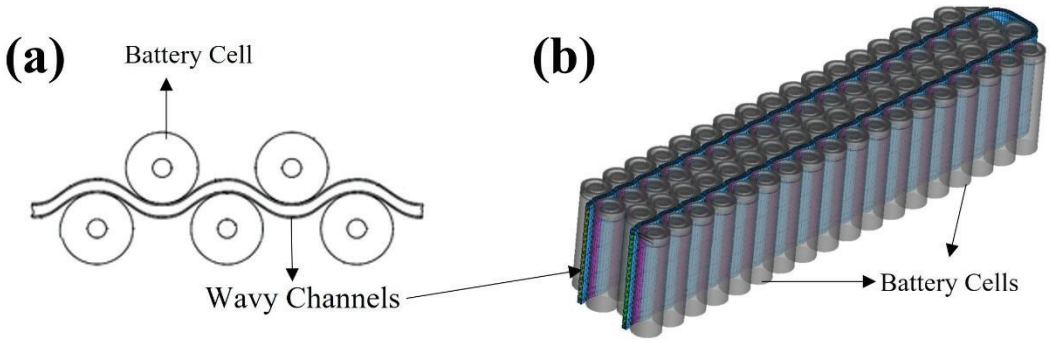

Figure 2.6. (a) The schematic of the wavy channel [97] (b) The schematic of the battery pack using wavy channels [99].

Zhao et al. [99] studied the performance of the wavy channels around the cylindrical cells. They investigated the effects of C-rate, coolant flow rate, the interface between neighboring batteries, battery, and the outer channel wall, as shown in Figure 2.6(b). The results show that the wavy channel cooling (with 0.5m/s inflow velocity, 25°C inflow temperature, and 5C discharge/charge rate) the maximum temperature and temperature uniformity can be kept below 35°C and 1°C, respectively. Xu et al.[100] suggested and constructed a novel liquid cooling system with cold plates for a prismatic LiFePO4 battery module to enhance the thermal performance of the module at high ambient temperatures. The results received from the test at different temperatures and discharging rates show that cold plate-based liquid cooling provides adequate thermal performance and reduces the maximum temperature difference to 3.8°C. Panchal et al. [101] also developed a liquid-cooled BTMS using dual cold plates for 20Ah prismatic cells and investigated its performance at different C-rates and ambient temperatures. The results demonstrate that the highest temperature is observed at the end of discharge of 4C for the ambient temperature of 35°C. Basu et al. [102] introduced an indirect liquid coolant-based thermal management system for a 18650 cylindrical battery pack. They used aluminum conduction elements surrounding the cells between the aluminum channels carrying liquid coolant in order to transfer heat away through thermal conduction. The study shows that the maximum temperature rise can be kept around 7K for a 2.7C discharge rate and 0.01m/s inlet coolant velocity. Although the above studies claim to provide adequate cooling with partial surface contact, the thermal efficiency can be improved due to increasing heat transfer interface area as partial contact yields overcooled spots. The cooling strategy having increased contact surface area can be defined as more efficient in terms of thermal

management. Therefore, another option is to place cylindrical battery cells in the housings or similar structures of the module, and the coolant liquid passes through the external surface of these structures. Thus, the coolant leakage and electrical short are prevented as the thermal efficiency and temperature uniformity are increased. However, these additional structure causes the total weight of the battery pack to increase.

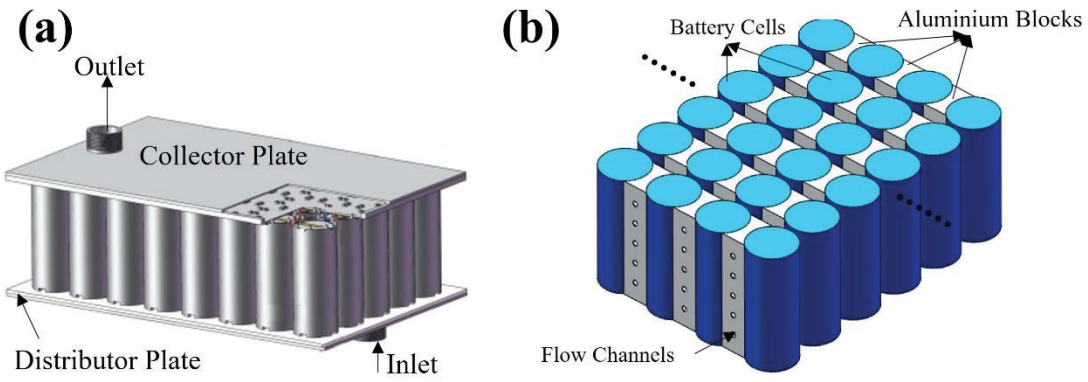

Figure 2.7. (a) the schematic of LCCs including 40 battery cells [103], (b) the schematic of the battery pack using cooling blocks with liquid channels [44].

Zhao et al.[103] numerically investigated the effects of the number of channels, mass flow rate, flow direction, and entrance size of the proposed cooling method (mini channel liquid-cooled cylinder, (LCC)) on the heat dissipation for cylindrical battery cells. Figure 2.7(a) showed the schematic of LCCs, including 40 battery cells. The results of simulations show that if the number of channels is a minimum of 4 and the inlet mass flow rate is 10^{-3} kg·s^{-1}, the maximum temperature can be kept below 40°C, although decreasing the temperature difference between the positive and negative poles is difficult in the LCC. In addition, the proposed cooling method with LCC can be defined as more favorable than natural convection cooling only when the number of channels is more than eight. Rao et al. [44] investigated the performance of BTMS with varying contact areas along the flow direction. Each aluminum block between the battery cells has five cooling channels shown in Figure 2.7(b). The heat conducted to blocks is transferred to the coolant by convection. The results show that the varying contact area cases provide better performance in terms of increasing temperature uniformity and decreasing maximum temperature and weight of battery module compared to constant contact area case.

Air and liquid cooling strategies are commonly complex, bulky, and need power-requiring components such as fans and pumps. On the other hand, the PCM cooling

strategy transfers the heat from the batteries by utilizing the latent heat of phase changing without using any additional components or systems. Compared to the active cooling methods, passive cooling methods such as PCM-based cooling are paid attention to due to their high potential to be a low-cost, effective, and simple thermal solution [62]. However, there are drawbacks, such as low thermal conductivity and volume changing during phase change. Therefore, highly conductive material addition, including carbon fibers, carbon nanotubes, graphene, metallic foam, and metal particles, is considered to improve the overall thermal conductivity [104].

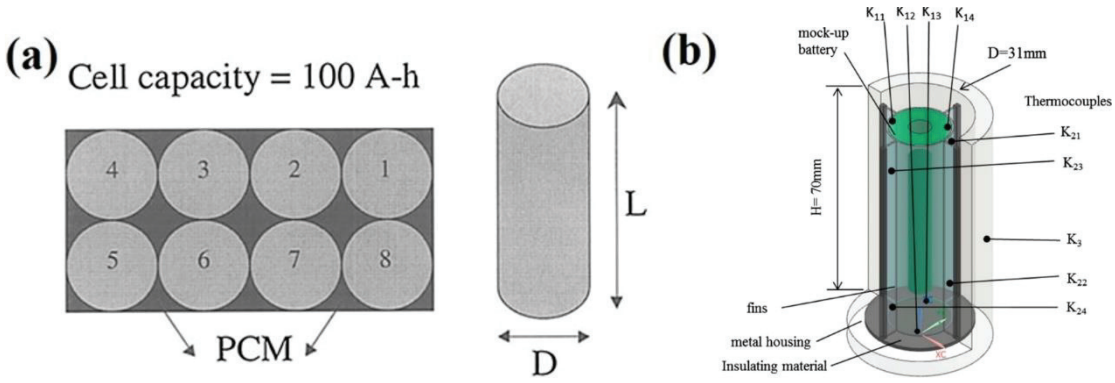

Figure 2.8. (a) The proposed PCM-based cooling EV module [105], (b) pcm with fin structure [106].

In the literature, one of the most popular and common investigation subjects is PCM-based cooling for BTMS applications. [41], [42], [107]–[109]. Initially, Al-Hallaj and Selman [105] suggested and patented BTMS based on PCM. They integrated the PCM within the battery module, as shown in Fig. 2.8(a). The results show that the temperature of 100Ah cell in a PCM integrated battery module at near-insulating conditions is reduced by approximately 8°C compared to the module without PCM. Sabbah et al. [110] compared the effectiveness of the active air cooling and passive PCM cooling methods. The results of simulations show that PCM-based passive cooling is more efficient than forced-air cooling. An efficient passive cooling strategy of a PCM embedded with copper metal foam was experimentally investigated by Khateeb et al. [111]. They showed that the use of aluminum foam/PCM composite resulted in an additional decrease in maximum temperature of about 5 °C compared to pure PCM for 2.2 Ah 18650 battery cell pack. Wang et al.[106] experimentally examined the thermal performance of a cooling approach (Fig. 43) using PCM with fin structure. Samimi et al.

[158] numerically studied the thermal performance of lithium-ion battery cells in the presence of PCM/carbon fiber composite and validated the results with experimental data. The study shows that the higher concentration of carbon fiber in the PCM increases the uniformity of temperature distribution and the average thermal conductivity enhancement of %105.

CHAPTER 3

MATERIALS AND METHOD

Despite the fact that there are numerous publications on battery pack thermal management, there is a scarcity of documentation on how battery packs should be designed to properly distribute coolant/air and maintain precise temperature control of the battery cells. Instead, the literature has been focused on improving manifold designs by analyzing random design characteristics or port placements. Here, we show how, with an enhanced battery pack design for advanced electric cars, all of the battery cells may be kept under the appropriate temperature by using a novel manifold design. The developed design aims to distribute fluid uniformly across battery cells by obtaining the same pressure drop along each flow channel. Second, the optimal design was simulated using the Newman, Tiedeman, Gu, and Kim (NTGK) electrochemical battery model, which, due to its heat production technique in a battery cell, delivers more realistic results. Finally, we compared the numerical findings to the outcomes of concept validation experiments.

3.1. Numerical Investigations

3.1.1. Numerical Model

Figure 3.1(a) illustrates the numerical solution domain where battery cells and air domains are represented in gray and transparent fashions, respectively. Figure 3.1(b) also includes the zoomed view of two distinct regions with their mesh elements. There are 15 battery cells that are compatible with the electric vehicle industry, i.e., modules with 6–24 cells are common.

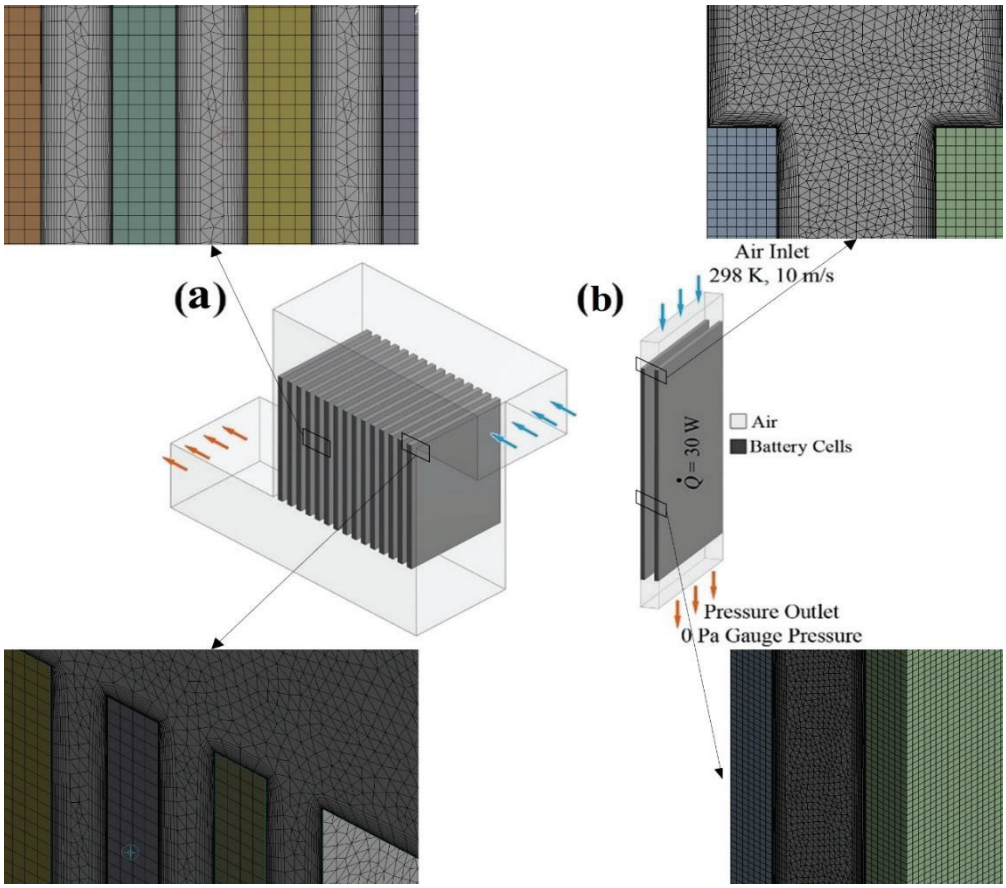

Figure 3.1. (a) Z-type manifold, and (b) elemental volume.

In addition, Fig. 3.1 documents the elemental volume representation of battery cells with spacing between them; the zoomed view of the meshed domains is also included. Coolant enters the Z-type manifold from the top at 10 m/s and 298 K and is distributed to the spacing between battery cells as shown in Fig. 3.1(a). Then, it is collected and leaves from the collector where the outlet boundary condition is zero gauge pressure. The design in Fig. 3.1(a) is of the Z-type because the coolant flows along a path that looks like Z, the inlet and outlet ports farther from each other and but the flow direction is the same. This manifold shape was selected due to its enhanced flow uniformity in comparison to the U-type designs [73], [113]. U-type manifolds have inlet and outlet ports on the same surface but the flow direction is the opposite of the inlet direction. This allows a major portion of the fluid to bypass cooling channels and flow directly from the inlet to the outlet.

Figure 3.1(b) indicates the boundary conditions for the elemental volume. Please note that conservation of energy is satisfied at the interfaces of battery cell surfaces and air. In order to document the effect of spacing between cells, the first numerical domains (two battery cells and air domain in between them) of Fig.3.1(b) was simulated. Thus,

simulation time was decreased greatly. Please note that the chief assumption is that the fluid is distributed uniformly (which is also going to be discussed) to each channel to uncover the minimum channel length required for effective cooling.

The fluid flow is assumed as incompressible because that the density change in the domain is negligibly small for all cases. In addition, it is assumed to be steady-state because the conditions are more challenging than many time-dependent case study conditions which indicates that the uncovered designs will be applicable for many distinct cases. Reynolds number is greater than the critical Reynolds number; therefore, the flow is turbulent. With all these in mind, the conservation o mass, momentum, and energy equations in averaged orm become [114], [115];

$$\frac{\partial \overline{u_J}}{\partial x_j} = 0 \tag{1}$$

$$\frac{\partial}{\partial x_j}(\rho \bar{u}_i \bar{u}_j) = -\frac{\partial \bar{P}}{\partial x} + \frac{\partial}{\partial x_j}\left[\mu\left(\frac{\partial \overline{u_i}}{\partial x_j} + \frac{\partial \overline{u_J}}{\partial x_i}\right)\right] - \frac{\partial}{\partial x_j}\left(\rho \overline{u_i{}' u_j{}'}\right) \tag{2}$$

$$\frac{\partial}{\partial x_j}\left(\rho \bar{u}_j \overline{T}\right) = \frac{\partial}{\partial x_j}\left(\frac{\mu}{\sigma_{cp}}\frac{\partial \overline{T}}{\partial x_j}\right) - \frac{\partial}{\partial x_j}\left(\rho \overline{u_j{}' T'}\right) \tag{3}$$

where $\rho, \bar{u}_i, \bar{P}, \mu$ are density, mean velocity component, fluctuating velocity component, mean pressure, and dynamic viscosity, respectively. k-ε turbulent model was chosen as viscous turbulent model due to its simplicity and validity in internal flows, that is

$$\frac{\partial}{\partial x_i}(\rho k \bar{u}_i) = \frac{\partial}{\partial x_j}\left[\left(\mu + \frac{\mu_t}{\sigma_k}\right)\frac{\partial k}{\partial x_j}\right] + -\rho \overline{u_i'} \overline{u_J'} \frac{\partial u_j}{\partial x_i} - \rho\varepsilon \tag{4}$$

$$\frac{\partial}{\partial x_i}(\rho \varepsilon \bar{u}_i) = \frac{\partial}{\partial x_j}\left[\left(\mu + \frac{\mu_t}{\sigma_\varepsilon}\right)\frac{\partial \varepsilon}{\partial x_j}\right] + C_1 \frac{\varepsilon}{k}\left(-\rho \overline{u_i'} \overline{u_J'} \frac{\partial u_j}{\partial x_i}\right) - C_2 \rho \frac{\varepsilon^2}{k} \tag{5}$$

$$\mu_t = \rho C_\mu \frac{k^2}{\varepsilon} \tag{6}$$

where $\mu_t, \varepsilon,\ k, C_\mu, \sigma_k$ and σ_ε are eddy viscosity, eddy dissipation rate, turbulence energy term, empirical coefficient and turbulent Prandtl numbers for k and ε, respectively, which are $C_\mu = 0.09, C_1 = 1.44, C_2 = 1.92, \sigma_k = 1\ and\ \sigma_\varepsilon = 1.3$ [116].

Table 1. Mesh independency results for the manifold model.

Number of Mesh Elements	Temperature Values [K]			Relative Error (%)		
	Outlet	Maximum	Mean	Outlet Temperature	Maximum Temperature	Mean Temperature
14140	305.124	338.574	318.278	–	–	–
44969	305.108	325.304	313.700	0.0053	3.9193	1.4383
153470	305.084	324.933	312.741	0.0078	0.1141	0.3058
300298	305.076	324.444	311.977	0.0028	0.1505	0.2443
352057	305.075	324.917	311.887	0.0003	0.1459	0.0290
401282	305.072	325.931	311.898	0.0009	0.3121	0.0036
480305	305.072	325.877	311.819	0.0001	0.0167	0.0252

The mesh is tetrahedral with inflation on battery cell walls. The mesh size was varied to uncover which mesh size yields results free of size effect. SIMPLE algorithm was used for pressure and velocity coupling. The convergence criterion for iterations is 10^{-6} for all the terms in the simulations. Table 1 shows the effect of mesh size on the outlet, maximum and mean temperatures and their relative errors. Mesh size was decreased until the relative error values became less than10^{-3}. Overall, mesh with approximately 4.8×10^{5} elements was chosen because all the relative errors become negligibly small, i.e. less than 0.03%.

Figure 3.2 shows that the volumetric flow rate along each channel in between two cells for our current approach as well as Park [74] and Chen et al. [73]. Overall, Figure 2 shows that the results of the current study are in agreement with the results of Park [74] and Chen et al. [73].

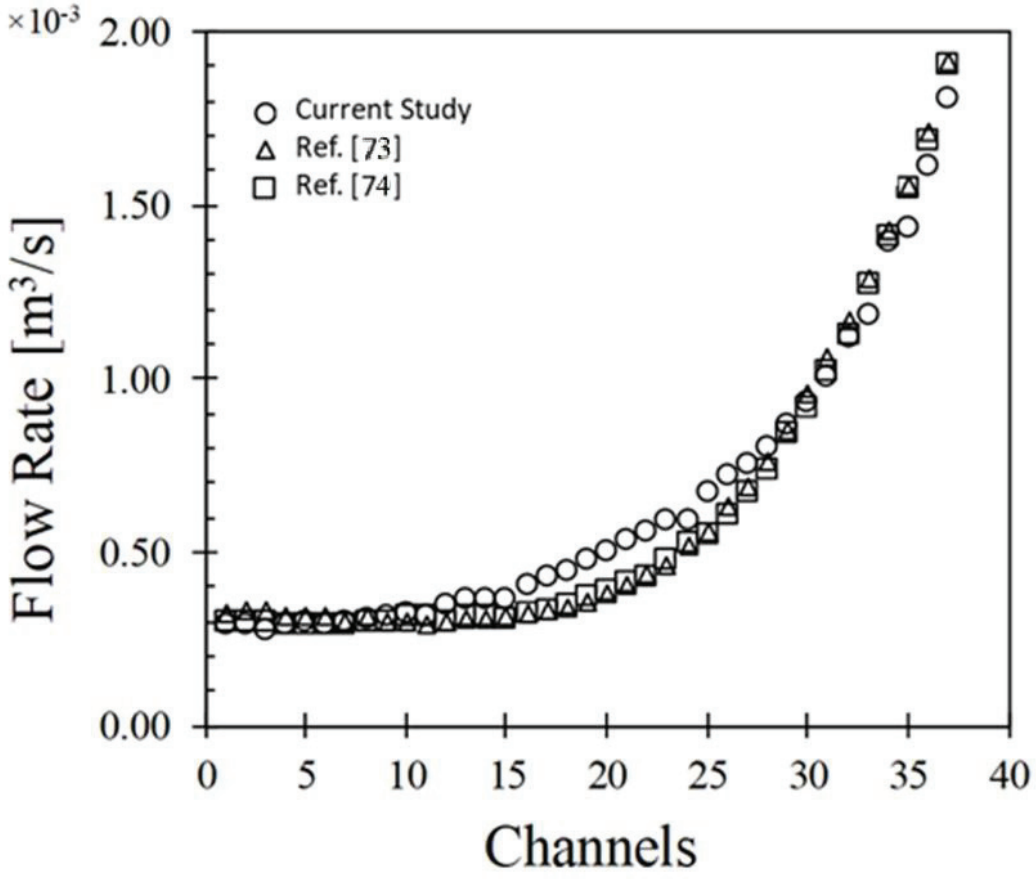

Figure 3.2. The results of the validation study.

In addition, satisfying the optimum operational temperature range in batteries is crucial for safety and extending battery life. Thus, it is a great advantage to have an estimation of heat generation of cells during discharge/charge during the development of advanced battery thermal management systems. Therefore, Newman, Tiedeman, Gu, and Kim (NTGK) semi-empirical electrochemical battery model was incorporated with multi-scale multi domain (MSMD) approach in ANSYS Fluent. The illustration and structural properties of the optimal manifold design, which will be discussed in detail, are given in Figure 3.3(a) and Table 2, respectively. Unlike the first numerical approach above, heat generation in cells is non-uniform and time-dependent as it relies on the electrochemical model incorporated with the thermal model.

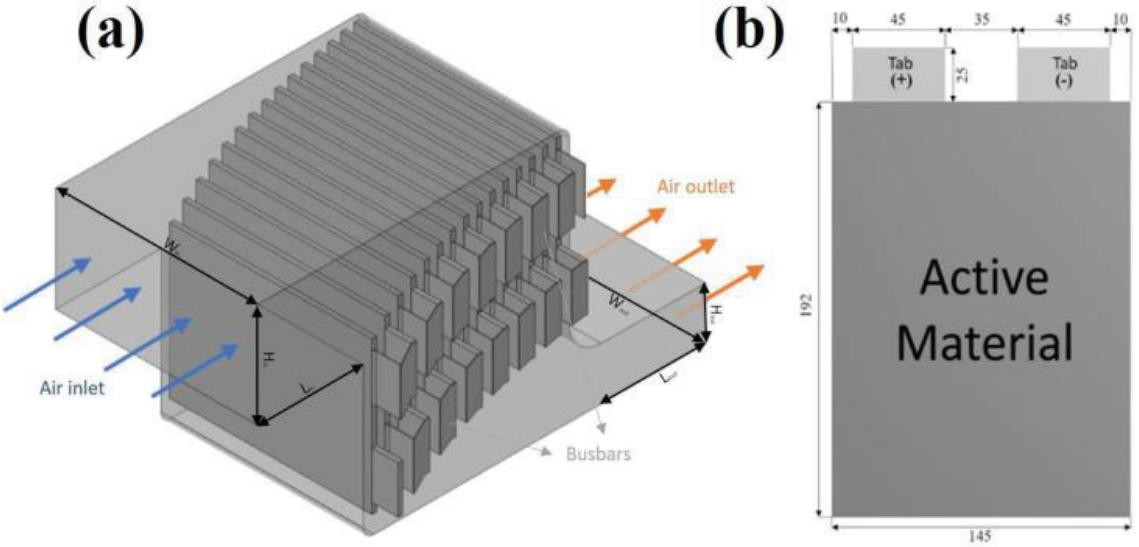

Figure 3.3. (a) Developed manifold design and (b) battery model domain.

Here, a three-dimensional model of a lithium-ion pouch cell with its geometry and dimensions are given in Fig. 3.3(b) was developed. The properties of the battery cell and cooling air are listed in Table 3. Then, using the same approach, the numerical model of the 7.5Ah Kokam cells in our laboratory was developed and compared with the experimental study.

Table 2. Structural properties of the manifold design.

Parameters	**Value [mm]**
Length of the inlet region (Lin)	100
Height of inlet region (Hin)	100
Width of the inlet region (Win)	192
Length of the outlet region (Lout)	100
Height of the outlet region (Hout)	50
Width of the outlet region (Wout)	192

Table 3. Physical properties of the battery cell and air.

Parameters	**Battery Cell**	**Air@298 K**
Density (kg/m3)	2092	1.184
Specific heat capacity (J/(kg.K))	678	1007
Thermal conductivity (W/(m.K))	18.2	0.02551
Dynamic viscosity (kg/(m.s))	-	1.149E-5
Size (mm)	7x145x192	-

In the electrochemical battery model formulation, the volumetric current transfer rate is defined by the following equation[39], [116]:

$$j_{ECh} = \frac{Q_{nominal}}{Q_{ref} Vol} Y \left[U - (\varphi_+ - \varphi_-)\right] \tag{7}$$

where $Q_{nominal}$ denotes total electric capacity of the cell, Q_{ref} is the capacity of the battery used in experiments, Vol describes volume of the active zone, φ_+ and φ_- terms are phase potentials for positive and negative electrodes. U and Y are the fitting parameters, and they are defined as a function of the battery depth of discharge (DOD)[117]. U and Y functions can also be determined by the curve that fits the voltage-current curve obtained from the experiments for a battery cell. In the formulation, the following equations were suggested by ANSYS Fluent[116]:

$$U = \left(\sum_{n=0}^{5} a_n (DoD)^n\right) - C_1\left(T - T_{ref}\right) \tag{8}$$

$$Y = \left(\sum_{n=0}^{5} b_n (DoD)^n\right) exp\left[-C_2\left(\frac{1}{T} - \frac{1}{T_{ref}}\right)\right] \tag{9}$$

where a_n and b_n are the constants obtained from experiments, C_1 and C_2 denote the NTGK model constants. The electrochemical reaction heat $\dot{q}_{ECh}$, which consists of electrochemical reactions in the model, is calculated as

$$\dot{q}_{ECh} = j_{ECh}\left[U - (\varphi_+ - \varphi_-) - T\frac{dU}{dT}\right] \tag{10}$$

where the first term represents heat due to overpotential and the other is heat based on entropic heating[116]. Regarding the NTGK battery model, the time term is added to the conservation equations, and also battery thermal and electrical fields were calculated in the numerical domain by the following equation [116]

$$\frac{\partial(\rho C_p T)}{\partial t} - \nabla.(k\nabla \mathrm{T}) = \sigma_+ |\nabla\varphi_+|^2 + \sigma_- |\nabla\varphi_-|^2 + \dot{q}_{ECh} \tag{11}$$

where T and λ are temperature and thermal conductivity, respectively. σ_+ and σ_- denote the effective electric conductivities for the positive and negative electrodes.

Table 4 shows the effect of mesh size on time-dependent simulations. In the mesh structure, two element types (hexahedral for the battery domain and tetrahedral for the flow domain) were used. The element size, inflation number, and layer thickness were varied in order to results to become independent of mesh size even for the regions where the gradients almost do not change. The effect of mesh size on the maximum temperatures of air at the outlet and batteries with relative errors can be seen in Table 4. Consequently, the mesh structure which has approximately 9822385 elements with 5 inflation layers (0.1 mm first inflation layer thickness) yields results free of mesh size, i.e. relative error less than 0.01%.

Table 4. Effect of mesh size on time-dependent simulation results.

	Temperature [K]		**Relative Error (%)**	
Number of Mesh Elements	Maximum Outlet	Maximum Battery	Maximum Outlet	Maximum Battery
863925	304.078	304.441		
1401807	302.448	302.855	0.5361	0.5208
5234692	303.150	303.143	0.2319	0.0950
8726784	303.200	303.198	0.0167	0.0181
9822385	303.334	303.315	0.0441	0.0387
12903540	303.315	303.332	0.0061	0.0056

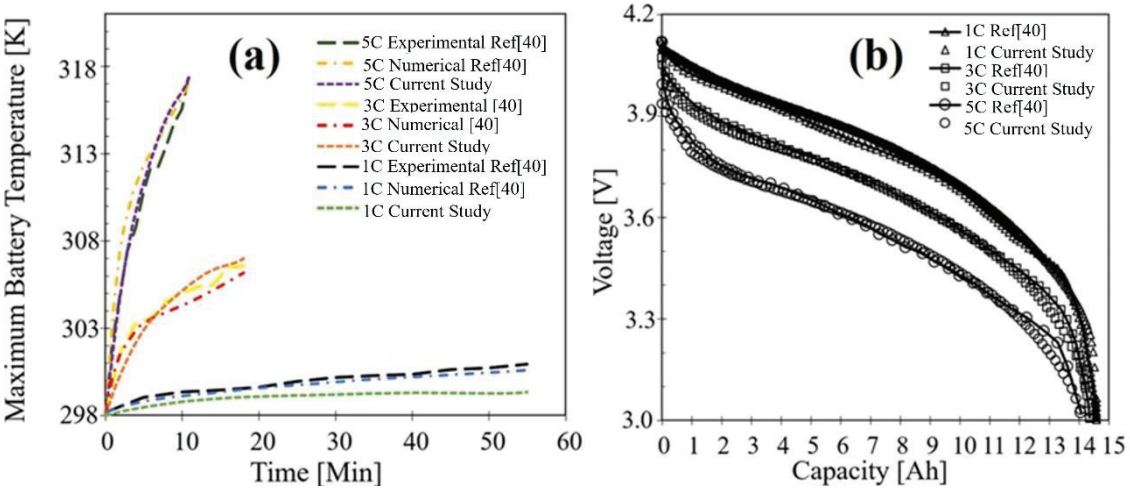

Figure 3.4. Comparison of (a) maximum battery temperatures and (b) voltage curves of Ref. [40] and current study for 1C, 3C, and 5C at 298K.

Current battery model results validated by the results of Kim et al.[40] where dimensions, materials, thermal and electrochemical properties are identical. The results of our numerical model were compared with the experimental and numerical data of their study. Figure 3.4(a) shows the maximum temperature change with respect to time and voltage-capacity curve for a single battery cell at 298K ambient temperature for three distinct C-rates: 1C, 3C, and 5C. For all discharge cases, the maximum temperature deviation from Kim's experimental and numerical data is ±1.5K, cf. Fig. 3.4(a). Moreover, the voltage-capacity curves show the results of the current study are in agreement with the results of Ref. 40, Fig. 3.4(b). These results show that our current numerical approach is valid.

CHAPTER 4

EXPERIMENTAL METHOD

4.1. Experimental Setup

To prove the accuracy of numerical studies and validate the developed manifold design, an experiment with the same design concept was established. As shown in Fig. 4.1, the experimental setup consists of manifold, batteries, electronic load, power supplier, axial fan, BMS, and data logger. In this section, all of the experimental setup will be explained.

In the experimental setup, a battery pack of 25.2 V and 7.5 Ah was designed by using 7.5 Ah Kokam pouch cells connected as series and controlled by a battery management system. The specifications of the Kokam SLPB75106100 cell are given in Table 5. The batteries were placed into the manifold which was manufactured in two main parts by a 3D printer from abs plastic resistant up to 60°C. Then, the plastic parts were adhered together with epoxy and assembled with a nozzle made of the same material. GW Instek PSH-2018A power supplier was used to charge the battery pack and BK Precision 8614 electronic load was used for discharging processes. The temperatures were measured by K-type thermocouples and recorded by HIOKI-LR8431-20 datalogger. The thermocouples were placed on the center of each cell, in inlet and outlet regions of the manifold, and also in ambient Bi-sonic 120 × 120 mm tube-axial fan was integrated with honeycombs to provide cooling air with the measured air velocity of 2.5m/s.

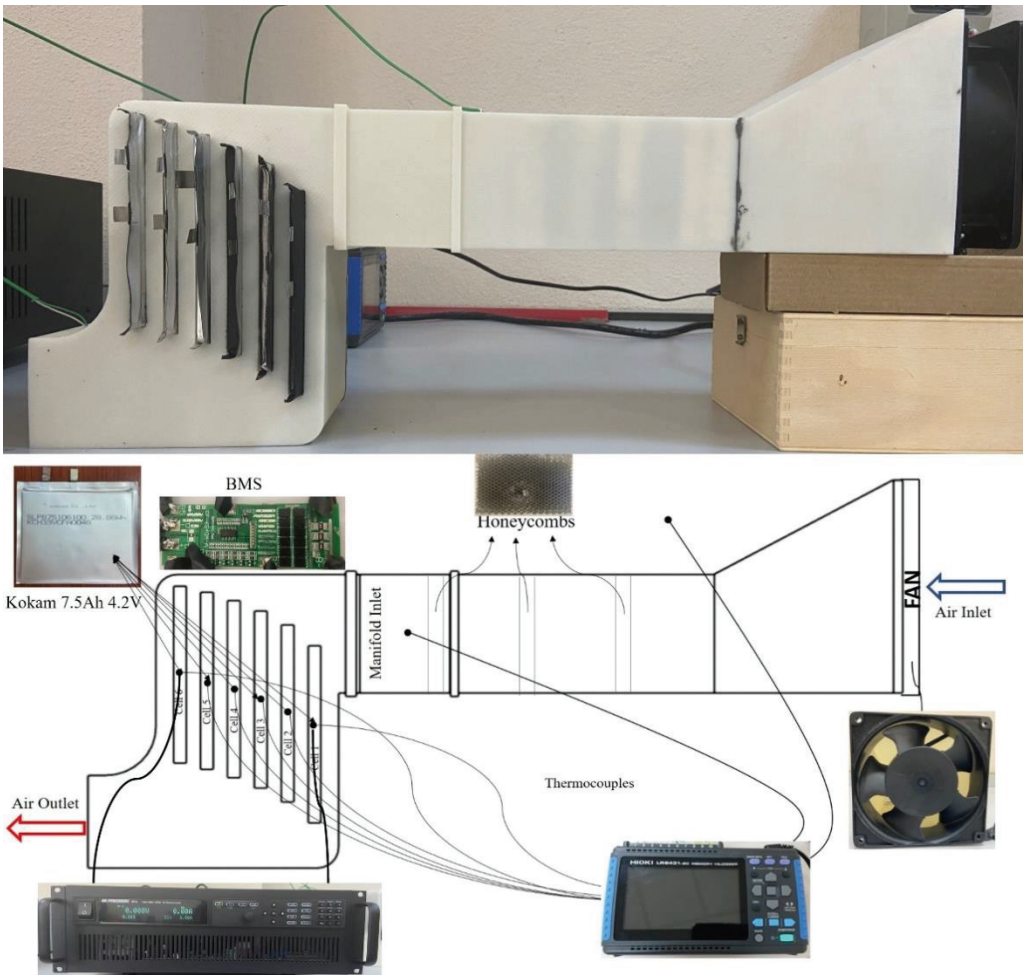

Figure 4.1. (a) Picture and (b) schematic of the experimental setup.

Table 5. Specifications of SLPB75106100.

Items	**Specifications**			Remarks
Rated Capacity	7.5 Ah			Charge @0.2C, 23±3°C Discharge @0.2C, 23±°C
Voltage	Minimum		2.7V	
	Maximum		4.2V	
Current [Max.]	Charge	Cont.	15A (2C)	@ 23±°C
	Discharge	Cont.	37.5A (5C)	@ 23±°C
Energy Density	168 Wh/kg			
Impedance	Max. 4.0 mΩ			AC @1kHz
Weight	Max. 165g			
Cell Dimension	Width		107 mm	Side seal folding
	Length		102 mm	Except fort tab length
	Thickness		7.9 mm	

4.2. Experimental Procedure

Lithium-ion battery charging and discharge operations must be carefully planned and implemented to ensure the efficiency and safety of batteries. Previous studies have shown that, even when the same C rate is utilized, the cell life of a lithium-ion battery is significantly influenced by the intended charging procedure[118]. Critical difficulties such as sudden capacity loss, short circuits, overcharging or discharging, leakage, and structural issues can arise if the operating processes are not properly established and applied to the cell. Before the performance tests at the module level, the cell characterization tests were conducted for each cell. Table 6 shows the steps in the characterization procedure that are used in the current study. The characterization operation is carried out at a constant ambient temperature of 300K. In the first step, batteries have been charged with constant current of 7.5 A (1C) up to 4.2V. When the battery reached 4.2 V, the charging process continued at constant voltage until the current value was decreased to 0.375A (1/20C). The idle period between the first and second steps is one hour. The second step involves discharging with constant current of 7.5A (1C) to the cutoff voltage of 2.7V. In the last step, the cells were completely charged with the same procedure in the first step. and then discharging at 1C until reaching to 2.7V cut-off voltage. The batteries are ready to be tested under certain conditions once the characterization operation is completed. During the single-cell tests, ambient and cell temperatures were recorded with K-type thermocouples which are connected to the HIOKI LR8434-20 datalogger and Testo 885-2 thermal camera.

Table 6. Characterization Procedure.

Step	**Process**	**Duration** (h)	**Current** (A)	**To/Until**	**Idle time** (h)
1	Charge	1.5	7.5	4.2V/0.375A	1
2	Discharge	0.9	7.5	2.7V	1
3	Charge	1.5	7.5	4.2V/0.375	1

In the experiment, six identical 7.5Ah Kokam pouch cells were placed in the manifold to conduct module-level performance test under discharge rate of 2C at ambient temperature of 300K. Temperature variations were recorded by datalogger with thermocouples placed in the center of each cell. Then, the air was driven by an axial fan and has flowed through the channels between cells. The discharging process was

conducted by electronic load after providing temperature balance between cells and ambient. The process is terminated when the battery pack voltage reaches the cut-off value of 16.2V.

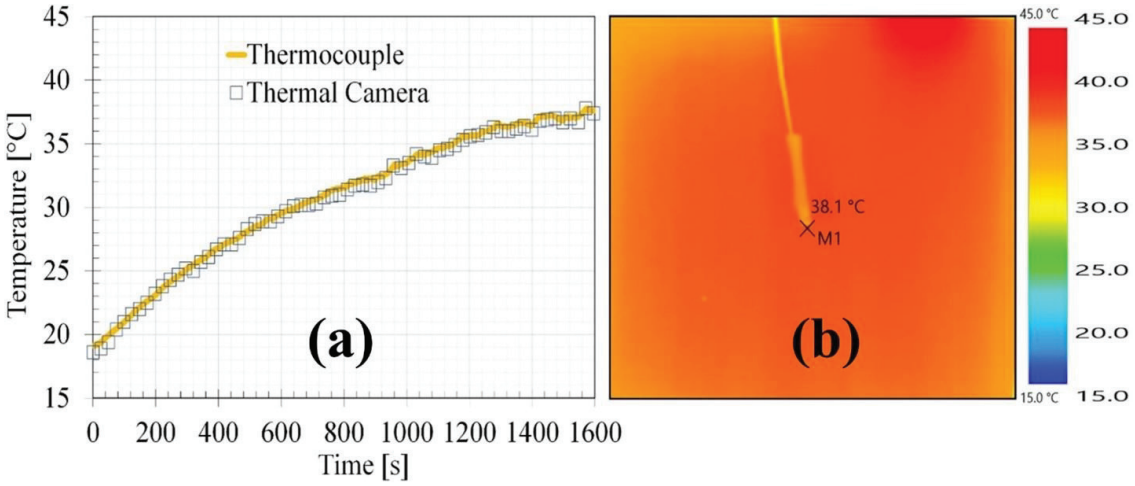

Figure 4.2. (a) Comparison of time-dependent temperature data measured with the thermal camera and thermocouples, (b) thermal image of the cell at the end of discharge of 2C.

To estimate the accuracy of both thermocouple and thermal camera measurements, time-dependent temperature changes during discharge of 2C on the battery were recorded comparatively with K-type thermocouples and thermal camera. Figure 4.2(a) shows the comparison of time-dependent temperature data obtained with the thermal camera image and thermocouples, and Figure 4.2(b) shows the thermal camera image at the end of discharge. The results show that the temperature trend obtained by the two measurement methods during discharge has a maximum deviation of 1.61%. This proves that the measurements made with both the thermal camera and the thermocouples are in good agreement with each other and under the calculated experimental error range.

CHAPTER 5

RESULTS AND DISCUSSION

5.1. Numerical Results

5.1.1 Spacing Between Battery Cells

Literature shows that spacing in between heat generating domains can be optimized when they are packed into a finite space[24]. Accordingly, first, we survey what should be the optimal spacing in between each Li-ion battery cell to achieve effective thermal management with maximum possible energy density in the battery pack. Figure 3.1(b) shows that air enters to an elemental flow volume in the pack with inlet velocity and temperature of 10 m/s and 298 K. Then, it sweeps the surfaces of the battery cells and leaves where the outlet pressure is zero gauge pressure. The heat generated volumetrically in each battery cell with the magnitude of 30W [119]–[122]. This volumetric heat generation rate corresponds to the maximum heat generation for 14.6 Ah battery cell under 5C discharge [119]. The change in the air temperature at the outlet can be calculated from

$$\dot{Q} = \dot{m}.c_p.(T_{out} - T_{in}) \tag{12}$$

Table 7 documents air outlet temperature calculated analytically (Eq. 12) and numerically are in agreement. This also shows that the current model is valid. In addition, Table 7 shows that the change in outlet temperature becomes less than 0.5 K as the spacing increases from 7 to 9 mm. Furthermore, the outlet temperature stays almost the same from 9 to 13 mm spacing.

BTMS should be as compact as possible in order to satisfy the requirements of advanced vehicles, i.e. maximum possible energy density with uniform temperature distribution. The spacing which performs almost as well as the best one with the smallest

possible distance is 8 mm. Therefore, spacing in between the battery cells is selected as 8 mm throughout this study.

Table 7. The effect of distance between battery cells.

Distance [mm]	Reynolds Number	Outlet Temperature Eq. (7) [K]	Outlet Temperature (Numerical) [K]	Error (%)
3	3557	303.17	303.54	0.1206
5	5855	301.10	301.56	0.1511
7	8098	300.21	300.51	0.0974
8	9198	299.94	300.15	0.0699
9	10286	299.72	299.79	0.0218
11	12422	299.41	299.40	0.0036
13	14508	299.19	299.24	0.0153
16	17547	298.17	297.95	0.0746

Consider the base design of Fig. 5.1(a) with 15 pouch cell batteries and constant diameter distributor and collector channels. The coolant is distributed to the channels in between battery cells to keep their temperature at the desired level. Nonetheless, Table 1 shows that the fluid is distributed non-uniformly along the channels with constant diameter pack design. Thus, temperature distributions are not expected to be symmetric for each elemental volume, i.e. some battery cells would exceed acceptable temperature levels where others would be a lot colder than the rest. However, the temperature of the cells can be in the same order if flow rate distribution becomes uniform.

Figure 5.1(a) shows the pressure distribution for the base design with channel numbers. The figure shows that the pressure gradients in between the entrance and exit of each channel vary greatly. This also explains why the flow rate along each channel is distinct. In addition, Fig. 5.1(b) shows the flow rate for each channel and their deviation from the average flow rate for two- and three-dimensional models. The flow rate becomes 64.9% less and 73.4% more than the average flow rate for the channel with the flow of minimum (channel #1) and maximum (channel #16) with two-dimensional simulations. In addition, Fig. 5.1(b) shows the maximum flow rate is 5 times greater than the minimum flow rate. Overall, Figure 3 shows that fluid uniformity can be achieved if the pressure gradient for each channel becomes in the same order. In addition, Fig. 5.1 shows that the results of two- and three-dimensional models are in good agreement. The validity of the two-dimensional solution approach was uncovered with the three-dimensional model with the geometry of Fig. 3.1(a). Therefore, here we handle an iterative exhaustive search

design process with two-dimensional simulations in order to save time. However, verifying whether the flow uniformity is achieved with two-dimensional end design may require three-dimensional solutions to achieve desired flow uniformity. Please note that here exhaustive search design parameters are decided in each solution from the information supplied from the previous iteration. Consequently, the process here is not based on trying arbitrary parameter changes in an iterative process which accelerates the design process by decreasing the required number of solutions.

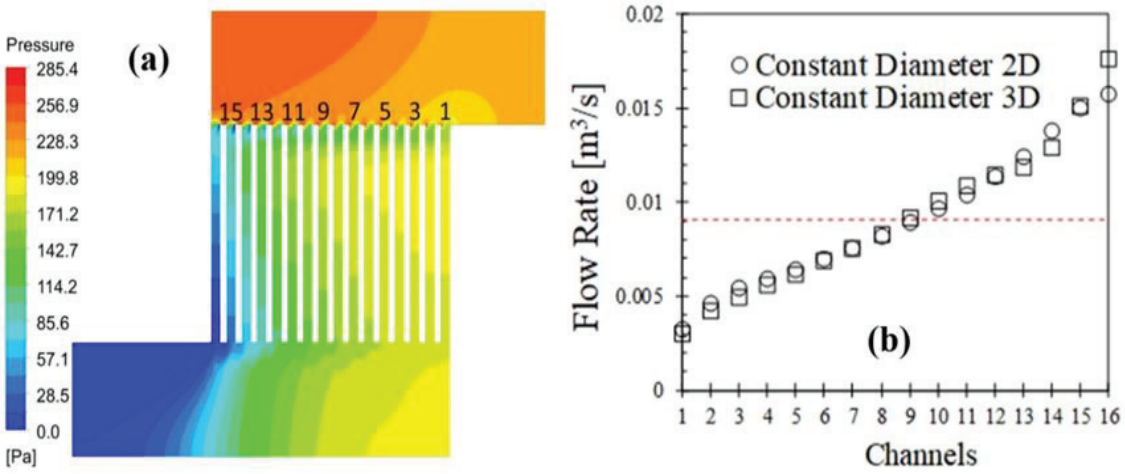

Figure 5.1. (a) Pressure distribution of base design and (b) flow rate along each channel.

Furthermore, in order to uncover the effect of flow rate magnitude on temperature distribution of battery cells, the energy equation was solved with conservation of mass and momentum equations for minimum, intermediate, and maximum flow rates values from the base design of Fig. 5.1(b), Figs. 5.2 (a), (b) and (c), respectively. Therefore, the accuracy of the two-dimensional and elemental volume approach can be further validated which is essential due to their small computational cost relative to the three-dimensional battery pack simulations. Comparison of Figs. 5.2(a) and 5.2(b) show that the maximum battery temperature decreases 11.33K from channel #1 to #9 (with minimum and intermediate flow rates, respectively). Yet, the battery temperature difference between channel #9 and #16 (intermediate and maximum flow rates, respectively) is 2.15K as shown in Figs. 5.2 (b) and 5.2 (c). These results show that the peak temperature in battery cells is affected greatly by flow rate non-uniformity. The peak temperature difference between distinct cells increases as the flow rate becomes greater or smaller than the average flow rate. Accordingly, Fig. 5.2(a)-(c) shows that fluid uniformity is essential in order to keep battery cell temperatures the same in a pack.

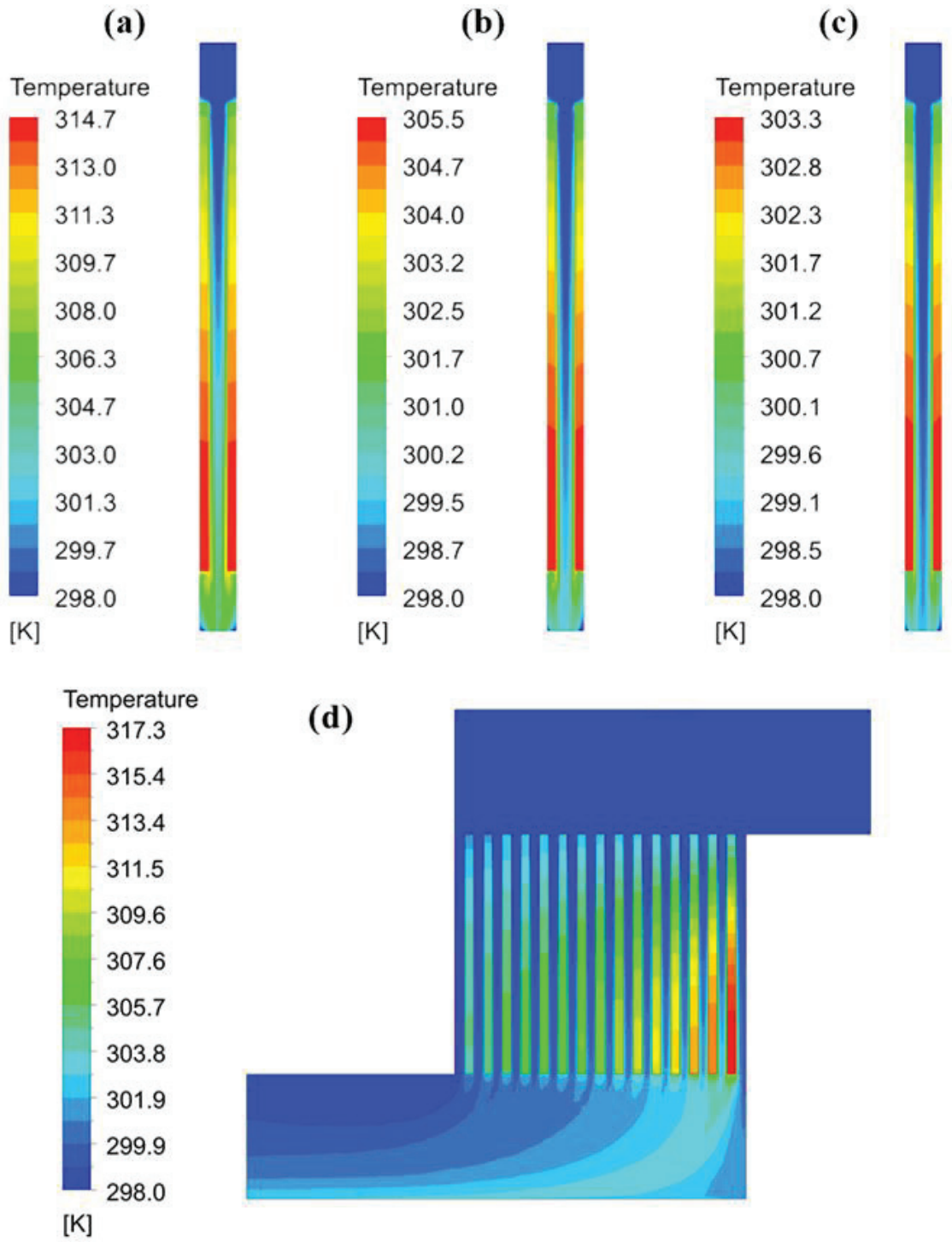

Figure 5.2. Temperature distribution of battery cells for (a) minimum flow rate (0.0032 m3/s), (b) intermediate flow rate (0.0089 m3/s), (c) maximum flow rate (0.016 m3/s), and (d) temperature distribution of 3D constant cross section design of Fig. 3.1(a).

In addition, Figure 5.2(d) shows the temperature distribution in the pack for the three-dimensional solution domain of Fig. 3.1(a). Comparison of Figs. 5.2(a), (b), and (c) with Fig. 5.2(d) shows the accuracy of the two-dimensional solution approach relative to

the three-dimensional one in terms of the flow of heat. The temperature difference values are almost the same in the elemental volume approach with the three-dimensional model of the pack. However, the maximum battery cell temperature is greater in Fig. 5.2(d) relative to Fig. 5.2(a) as expected because Fig. 5.1(b) shows that the flow rate along the first channel near the inlet is overestimated in the two-dimensional model. This result shows that optimizing geometric parameters in a two-dimensional model with the consideration of flow uniformity yields the design of a battery pack with uniform temperature distribution inside of it. Hence, computational time decreases greatly in the exhaustive search design procedure.

5.1.2. Uniform Flow Rate Distribution

In order to have constant pressure gradient along each channel, the shape of the manifold can be modified. For instance, the diameter of the distributor channel can be contracted as in Figs. 5.3 (a) and (b). Figure 5.3(a) documents how the pressure distribution varies if the distributor channel is contracted linearly. Figure 5.3(a) shows that the variation on the pressure gradient along each channel becomes more uniform than Fig. 5.1 but it is still not as uniform as desired. Especially, the pressure gradient is a lot smaller in the first channels (#1-4). Therefore, the contraction is steeped for the first channels, Fig. 5.3(b). This sudden contraction decreases the variation on the pressure but not in the desired level as well. Figure 5.3(c) shows how the volume flow rates are distributed along each channel for the designs of Fig. 5.3(a) and (b). Figure 5.3(c) also shows that the sudden contraction design performs slightly better except for the last two channels (channel #15 and #16). This shows contraction enables flow rate distribution uniformity but linear or sudden contraction does not satisfy the desired uniformity requirement. Consequently, it can be concluded that the design complexity should be increased in order to achieve uniform flow rate distribution.

A new and more complex (requires more geometrical parameters) manifold design, tapered design, was developed with Constructal design approach in order to distribute coolant along the channels more uniformly. The distributor channel has a sudden contraction at first, and then it is tapered gradually to enhance flow rate distribution uniformity as the results in Fig. 5.3 implies.

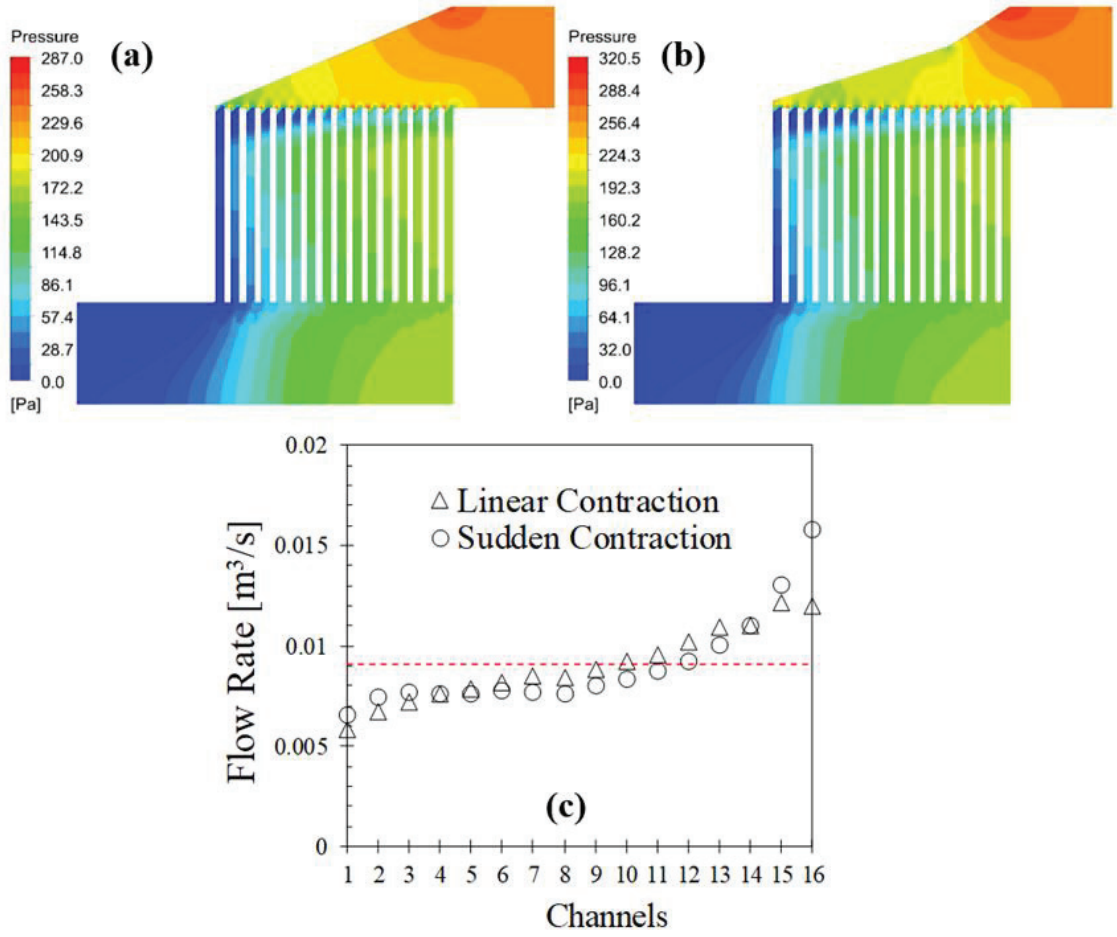

Figure 5.3. Pressure distributions of (a) linear contraction and (b) sudden contraction designs and (c) flow rate along each channel.

Fig. 5.4(a) shows how the pressure distribution is affected by tapering the distributor channel. The pressure gradient (flow resistance) along each channel decreases relative to the previous design of Fig. 5.3(b) (except the last two channels, #15 and #16) which have a sudden contraction. However, overall pressure drop increases in the design of Fig. 5.4(a) relative to the designs of Fig. 5.3 because of the increment in the fluid flow resistance along the distributor channel. Please note that the distributor is tapered gradually with linearly contracted channel size along the sections where fluid enters to channel. Flow rate is more uniform with the design of Fig. 5.4(b) relative to the design of Fig. 5.4(b) except channels #15 and #16. In addition, Fig. 5.4(b) also documents maximum and minimum flow rates are 122.3% more and 20.3% less than the average flow rate (channel #16 and #4, respectively.)

Tapered design of Fig. 5.4(a) was inspired from our previous work of Ref. [79] which was developed for a micro device. Nonetheless, manufacturing variable cross-section channels are not common due to their complexity. The reason why tapering

channel cross-section yields better flow uniformity is that the pressure gradient along the inlet and outlet of each channel located in between the cells can be kept at a constant value. Constant pressure gradient conforms to homogeneous coolant distribution. The pressure gradient between distributor and collector channels can also be fixed with constant manifold designs as the height of coolant channels embedded into the manifold vary. Manifold is constant in cross section where the vertical position of battery cells are dispersed exponentially as shown in Fig. 5.4(c), i.e. elevated design. The deviation in the flow rate relative to the average flow rate in channels #15 and #16 are reduced to 23.2% and 54%, respectively.

In addition, the comparison of Figs. 5.4(b) and 5.4(d) show the flow rate is distributed more uniformly in elevated design relative to the tapered one. The comparison of Figs. 5.4(a) and 5.4(c) uncover that the pressure drop also decreases as the elevation of battery cells is varied rather than altering the design of the distributor. However, maximum and minimum flow rates are 23.6% more and 8% less than the average flow rate for channels #8 and #5, respectively, which are more than the desired level. In addition, Figure 5.4(c) shows that the collector channel becomes very thick near the exit. This fluid domain is excessive, and it increases the pack volume without any purpose. Therefore, the elevated design can be modified by removing the excessive volume of the collector channel. This yields the energy density of the battery pack to enhance greatly, which is essential as the space reserved for the pack is limited. Next, consider the constructal design with the excess fluid domain near the exit of the manifold is subtracted as shown in Fig. 5.4(e). In addition, sharp corners near the inlet and outlet were rounded to get rid of sudden pressure drops. The vertical positions of batteries were optimized iteratively where the stop criterion was a maximum 1% fluctuation in flow rate relative to the average value. In order to achieve this criterion, the design was iteratively altered approximately 60 times. Battery positions in the initial design are the same with Fig. 5.4(c), 1st design. Yet, Figs. 5.4(d) and (f) shows that flow rate distribution becomes worse as the excessive volume near the outlet port is subtracted. It is expected as fluid flow along each channel is governed by the pressure difference in between the inlet and outlet of each channel. Varying geometrical parameters at the collector channel affect the pressure distribution along it, so the flow rate uniformity.

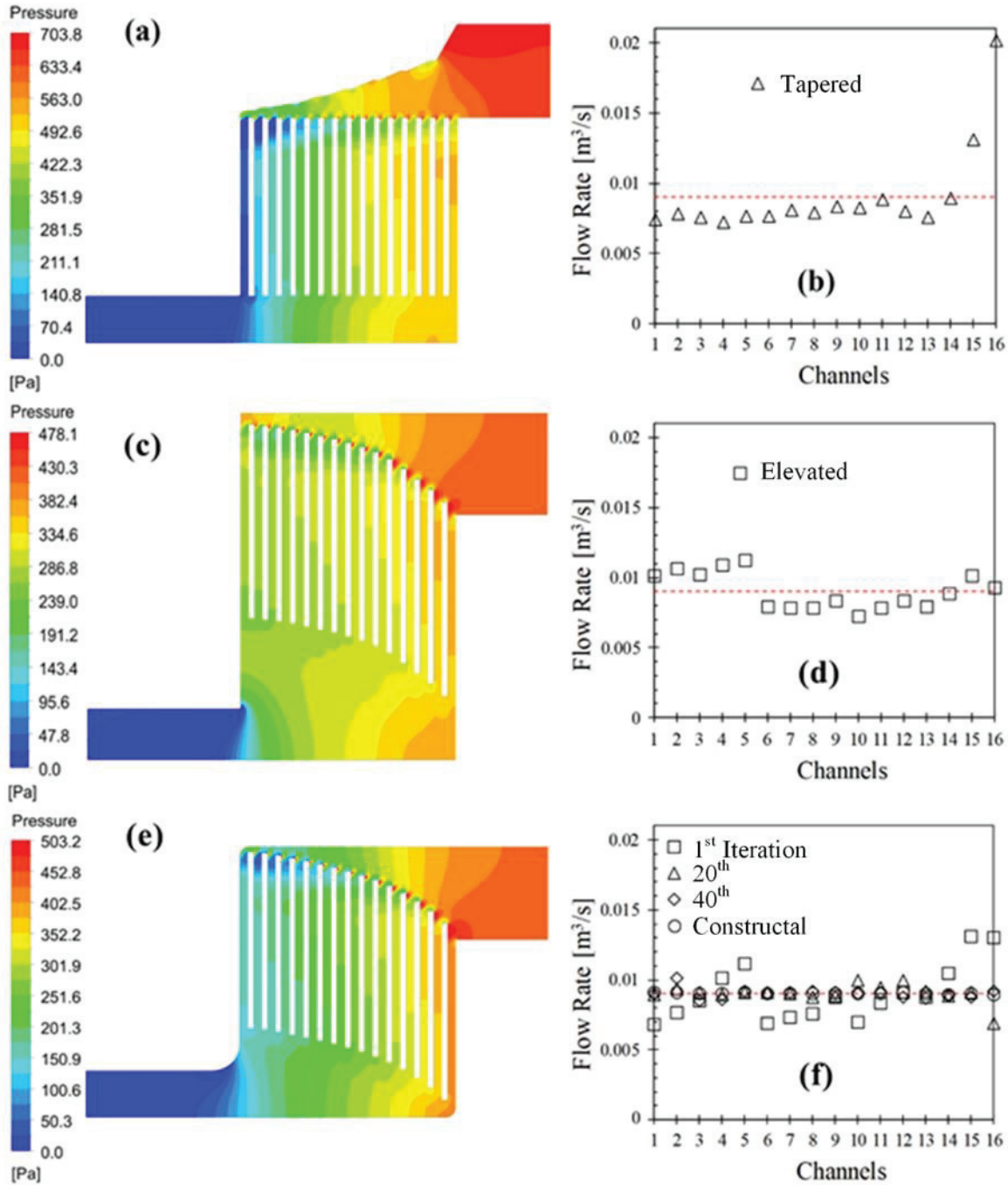

Figure 5.4. Pressure distributions and flow rate variations of (a) and (b) tapered design, (c) and (d) elevated design, and (e) and (f) constructal design, respectively.

Fig. 5.4(f) shows how flow rates along each channel evolve as the design is altered via the iterative exhaustive search method. Figure 6(f) documents flow rate distribution for first, twentieth, fortieth, and last iterations, i.e. constructal design. Moreover, the flow rate in between the channels is almost the same, the maximum flow rate deviation from the average flow rate is %0.81 (channel #5), Fig. 5.4(f). Figure 5.4(e) also shows the pressure distribution for constructal design. The pressure distribution along the distributor

and collector channels varies greatly. Nonetheless, the pressure gradient along the cooling channels does not vary as much as in tapered and elevated designs. Note that the required pressure increased approximately 200 Pa in the constructal design of Fig. 5.4(e) relative to the design of Fig. 5.1(a). The reason for this increment is due to the fluid is forced to flow uniformly along each channel in Fig. 5.4(e), there is no bypass channel as in the design of Fig. 5.1(a) where most of the fluid was flowing in several channels due to relatively less flow resistance in comparison to the other channels. The designs in Fig. 5.4 indicate that the flow uniformity requires increment in the pressure drop relative to the base design of Fig. 5.1.

5.1.3. Homogeneous Temperature Distribution

Results of Figs. 5.1 and 5.2 documented that the two-dimensional solution approach is useful to uncover flow rate uniformity but it lacks in documenting temperature distribution accurately. Thus, three-dimensional model of the battery pack with the cell positions of constructal design, Fig. 5.5(a), was simulated. Three-dimensional simulation confirms that the flow rate distribution calculated with two-dimensional simulations is valid, i.e. maximum variation in flow rate is 13.28% for the last two channels and maximum of 4.67% for the remaining channels, Fig. 5.5(b). Figure 5.5 also documents that the maximum temperature difference on a single battery is 7K (it is 5.5K for the majority of battery cells). These values stay in the acceptable operating temperature range. Comparison of Figs. 5.2 and 5.5 show cooling the cells in a battery pack can be achieved with the novel methodology of this study, i.e. locating the battery cells such that the pressure drop along each path line is the same to conform uniform coolant distribution. The novel approach yields the same temperature distribution for each cell in a pack. So, the temperature in a pack can be regulated strictly with this approach.

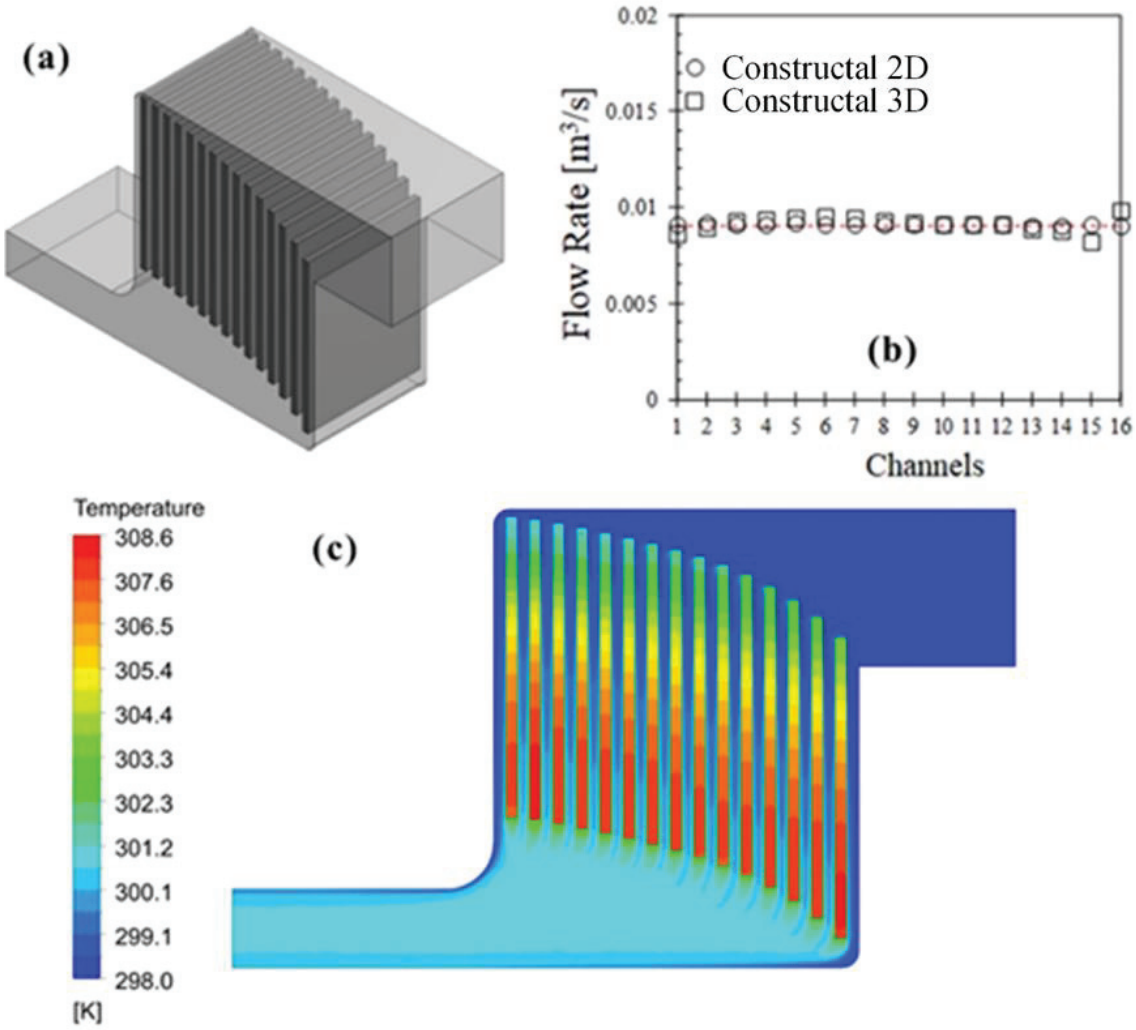

Figure 5.5. Three-dimensional model of the battery pack with the cell positions of Figs. 6(f) and 6(b) flow rate along each channel for two- and three-dimensional constructal models and (c) temperature distribution of the three-dimensional constructal model.

However, Figure 5.5 shows there is a mismatch between two- and three-dimensional solution methods as expected due to the results of Fig. 5.2. Even though it is relatively small, if this mismatch is eliminated temperature distribution can be more uniform along each battery cell. Therefore, the design of Fig. 5.5 is further improved with iterative exhaustive search by using three-dimensional models. The tenth iteration yields the design with the desired flow rate uniformity as the initial design almost satisfied flow uniformity, as can be seen in Fig. 5.6. The maximum temperature difference between the peak temperatures of battery cells become less than 0.5K and the maximum temperature difference on a single battery vary in between 6 – 6.5 K. Overall, processing cost has decreased greatly by uncovering battery locations corresponding to the flow uniformity

first with two-dimensional simulations, and then using that one as initial design in the three-dimensional exhaustive search procedure.

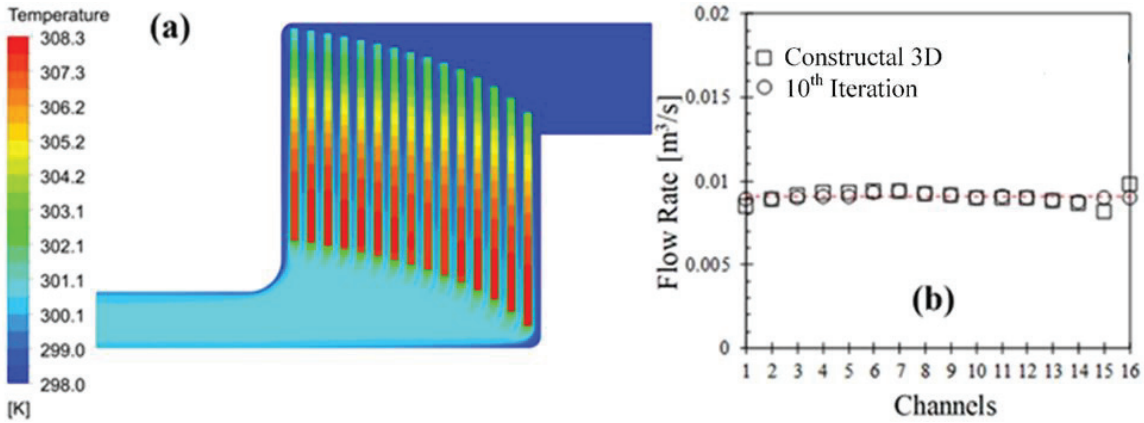

Figure 5.6. Temperature distribution of 10th iteration and (b) flow rate in each channel.

According to the results, constructal design performs much better than all other designs. Overall, this design can be defined as the best design in terms of flow rate distribution uniformity, decreased temperature difference (along batteries and in between them) and compactness compared to other competing designs.

Final numerical analysis was performed by using the validated battery model in the battery pack design, which provides homogeneous air distribution (Figure 5.6). In Figure 5.7, the temperature distribution of the developed manifold design using the NTGK battery model, which is time-dependent, at discharge rate of 5C, with fluid temperature of 298K and an inlet velocity of 10m/s, obtained from the 3D numerical analysis is given. Additionally, Figure 5.7 shows that the maximum temperature difference over a single battery is on average 1K, and the temperature distributions are approximately the same for each battery cell. The maximum difference between the maximum temperatures in the battery cells appears to be less than 0.5K. To sum up, Uniform flow rate distribution is focused as it reduces the maximum cell temperature and enhances temperature uniformity in the battery pack by eliminating under and overcooled regions.

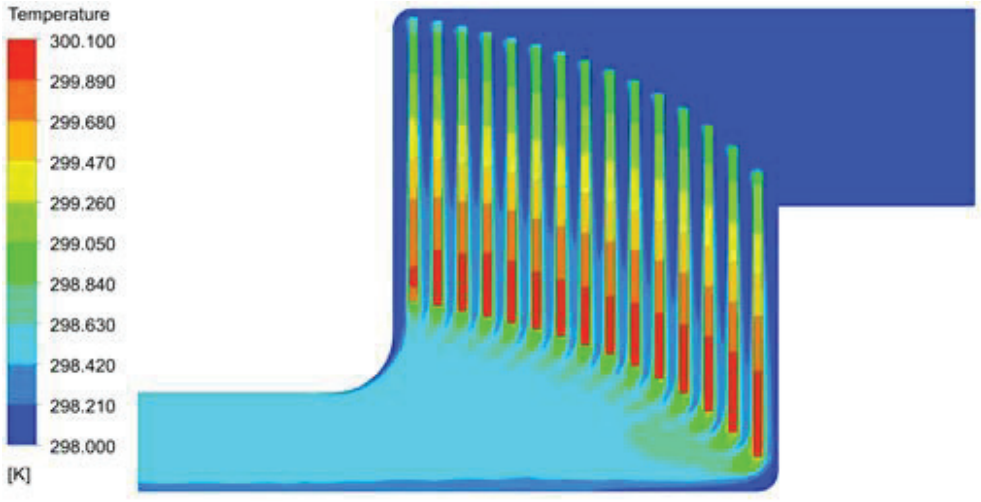

Figure 5.7. Temperature distribution of NTGK model integrated battery pack in the developed manifold at 10C discharge rate for ambient temperature of 298K.

5.2. Experimental Results

To validate the numerical studies and the developed manifold design, the concept validation experiments were conducted under a certain procedure mentioned in Chapter 4. The battery pack was discharged with the BK Precision 8614 programmable electronic load under 2 C-rate (15A) at an ambient temperature of 300 K, and the temperature data of each cell was recorded during the discharge process. the numerical analysis of the experimental setup in which Kokam cells were used was also performed by following the same method as the electrothermal battery model verified in numerical studies.

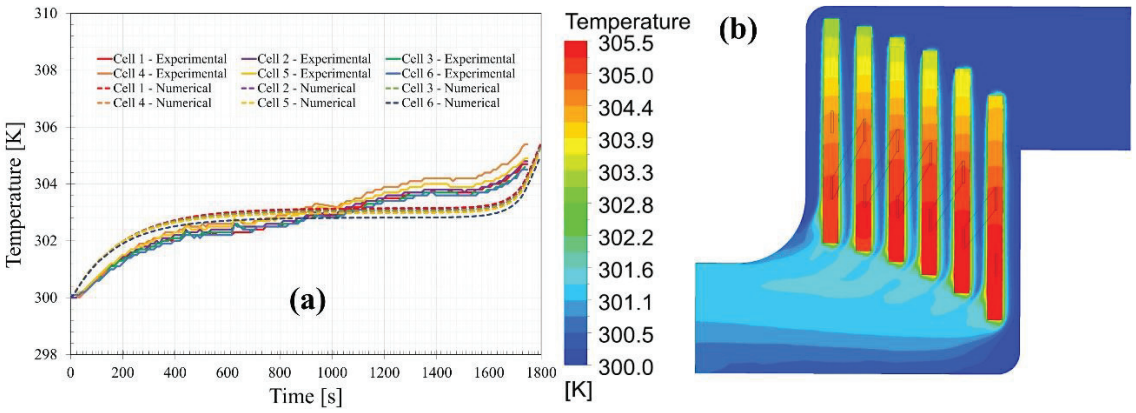

Figure 5.8. (a) Comparison of experimental and numerical temperature data, (b) temperature distribution of numerical study at end of the discharge process.

In Figure 5.8, numerical and experimental comparisons of the temperature variation of the cells during the discharge process and the temperature distribution of the batteries in the manifold at the end of the discharge are given. As can be seen in Fig. 5.8(a), experimental and numerical results are in good agreement with each other during operation. In the experimental study, the maximum battery temperature and temperature difference between the cells is measured as 305.4 K and 1 K, respectively. This result alone shows that the elevated battery positioning concept can provide uniform flow distribution between the cells and yields uniform temperature distribution in the pack. In addition, a comparison of experimental and numerical results shows that the deviation of maximum battery temperature is around 1.5 K (Fig. 5.8(a)-(b)) which heavily occurs near the end of the discharge process. Overall, experiments show that the elevated battery positioning concept yields temperature uniformity in the pack and the numerical procedure of the paper is valid and applicable.

CHAPTER 6

SUMMARY AND CONCLUSION

In this thesis, a new battery pack manifold design satisfying cooling requirements uncovered with enhanced compactness. In order to eliminate capacity loss and thermal runaway in battery cells, thermal management plays an integral role. The temperature difference in a battery cell should not be more than 5K to minimize aging, as the literature shows. However, the temperature difference between batteries is also essential and should be avoided as it affects the resistivity of cells directly and yield non-uniform charging/discharging characteristics. The results document that temperature differences in between and along battery cells can be minimized if the coolant is distributed uniformly along the channels located in between battery cells. First, the flow rate distribution of a base design was documented. The results show that the maximum temperature difference in a battery cell becomes 16.7K, as it would be 6K if the coolant was distributed uniformly. Then, the effect of linear and sudden contraction on the distributor channel was documented. The results show that the channel cross-section should be tapered with increased complexity. In order to satisfy this, a tapered design was introduced, and enhancement in the flow rate distribution was observed. Achieving a uniform flow rate by tapering the channel cross-section requires complex channel geometry which is difficult to manufacture. Next, collector and distributor cross-sections were kept constant, and the vertical position of battery cells was varied exponentially in elevated design. However, the elevated design includes an excessive flow domain without any purpose and sharp corners. Flow rate uniformity with less than 1% fluctuation was achieved by removing excess volume and rounding sharp corners. An experimental study was conducted to prove the validity of both numerical procedure and elevated battery positioning concept to achieve uniform temperature distribution. The results show that air cooling can be an effective thermal management system if an elevated battery positioning concept is used. The flow uniformity of air supplied to each cell is also essential for the applicability of metal-air batteries in battery packs. Therefore, the results of this paper can accelerate the usage of metal-air batteries in battery packs.

In addition, the results document that the two- and three-dimensional models are accurate, but there is a mismatch between them, specifically in temperature distribution. Consequently, the two-dimensional constructal design was used as the initial design for the three-dimensional optimization procedure. The results show that the temperature difference between the battery cells in a pack becomes almost the same (<1 K difference). Hence, strict temperature control of battery cells with the approach of this paper can be achieved. Overall, this thesis documents a compact BTMS design with uniform coolant distribution to eliminate thermal runaway and capacity loss in battery cells.

REFERENCES

[1] H. Jouhara *et al.*, “Applications and thermal management of rechargeable batteries for industrial applications,” *Energy*, vol. 170, pp. 849–861, Mar. 2019, doi: 10.1016/j.energy.2018.12.218.

[2] A. Foley and A. G. Olabi, “Renewable energy technology developments, trends and policy implications that can underpin the drive for global climate change,” *Renewable and Sustainable Energy Reviews*, vol. 68. Elsevier Ltd, pp. 1112–1114, Feb. 01, 2017, doi: 10.1016/j.rser.2016.12.065.

[3] H. Jouhara and A. G. Olabi, “Editorial: Industrial waste heat recovery,” *Energy*, vol. 160. Elsevier Ltd, pp. 1–2, Oct. 01, 2018, doi: 10.1016/j.energy.2018.07.013.

[4] A. Guterres, “Carbon Neutrality by 2050: theWorld’s Most Urgent Mission | United Nations Secretary-General,” *United Nations*, 2020. https://www.un.org/sg/en/content/sg/articles/2020-12-11/carbon-neutrality-2050-the-world’s-most-urgent-mission (accessed Sep. 28, 2021).

[5] IEA (2021), “Global EV Outlook 2021,” Paris, 2021. [Online]. Available: https://www.iea.org/reports/global-ev-outlook-2021.

[6] W. Wu, S. Wang, W. Wu, K. Chen, S. Hong, and Y. Lai, “A critical review of battery thermal performance and liquid based battery thermal management,” *Energy Conversion and Management*, vol. 182. Elsevier Ltd, pp. 262–281, Jan. 01, 2019, doi: 10.1016/j.enconman.2018.12.051.

[7] J. Kim, J. Oh, and H. Lee, “Review on battery thermal management system for electric vehicles,” *Applied Thermal Engineering*, vol. 149. Elsevier Ltd, pp. 192–212, Feb. 25, 2019, doi: 10.1016/j.applthermaleng.2018.12.020.

[8] J. Jaguemont, L. Boulon, and Y. Dubé, “A comprehensive review of lithium-ion batteries used in hybrid and electric vehicles at cold temperatures,” *Appl. Energy*, vol. 164, pp. 99–114, Feb. 2016, doi: 10.1016/j.apenergy.2015.11.034.

[9] S. Zhong *et al.*, “Recent progress in thin separators for upgraded lithium ion batteries,” *Energy Storage Mater.*, vol. 41, pp. 805–841, Oct. 2021, doi: 10.1016/J.ENSM.2021.07.028.

[10] T. Sasaki, Y. Ukyo, and P. Novák, “Memory effect in a lithium-ion battery,” 2013, doi: 10.1038/NMAT3623.

[11] P. R. Tete, M. M. Gupta, and S. S. Joshi, “Developments in battery thermal

management systems for electric vehicles: A technical review," *J. Energy Storage*, vol. 35, p. 102255, Mar. 2021, doi: 10.1016/J.EST.2021.102255.

[12] L. Ji, Z. Lin, M. Alcoutlabi, and X. Zhang, "Recent developments in nanostructured anode materials for rechargeable lithium-ion batteries," *Energy and Environmental Science*. 2011, doi: 10.1039/c0ee00699h.

[13] Y. Ji, Y. Zhang, and C.-Y. Wang, "Li-Ion Cell Operation at Low Temperatures," *J. Electrochem. Soc.*, vol. 160, no. 4, pp. A636–A649, 2013, doi: 10.1149/2.047304jes.

[14] X. Liu, Z. Chen, C. Zhang, and J. Wu, "A novel temperature-compensated model for power Li-ion batteries with dual-particle-filter state of charge estimation," *Appl. Energy*, vol. 123, pp. 263–272, Jun. 2014, doi: 10.1016/j.apenergy.2014.02.072.

[15] B. Scrosati and J. Garche, "Lithium batteries: Status, prospects and future," *Journal of Power Sources*. 2010, doi: 10.1016/j.jpowsour.2009.11.048.

[16] Q. Wang, B. Jiang, B. Li, and Y. Yan, "A critical review of thermal management models and solutions of lithium-ion batteries for the development of pure electric vehicles," *Renewable and Sustainable Energy Reviews*. 2016, doi: 10.1016/j.rser.2016.05.033.

[17] Z. Rao and S. Wang, "A review of power battery thermal energy management," *Renewable and Sustainable Energy Reviews*. 2011, doi: 10.1016/j.rser.2011.07.096.

[18] G. K. A. Pesaran , S.Santhanagopalan, "Addressing the Impact of Temperature Extremes on Large Format Li-Ion Batteries for Vehicle Applications," *30Th Int. Batter. Semin.*, 2013.

[19] X. Na, H. Kang, T. Wang, and Y. Wang, "Reverse layered air flow for Li-ion battery thermal management," *Appl. Therm. Eng.*, vol. 143, pp. 257–262, Oct. 2018, doi: 10.1016/J.APPLTHERMALENG.2018.07.080.

[20] P. Sun and X. Huang, "LLC, part of Springer Nature Manufactured in The United States," *Fire Technol.*, vol. 56, pp. 1361–1410, 2020, doi: 10.1007/s10694-019-00944-3.

[21] P. G. Balakrishnan, R. Ramesh, and T. Prem Kumar, "Safety mechanisms in lithium-ion batteries," *Journal of Power Sources*. 2006, doi: 10.1016/j.jpowsour.2005.12.002.

[22] Federal Aviation Authority, "EVENTS WITH SMOKE, FIRE, EXTREME HEAT

OR EXPLOSION INVOLVING LITHIUM BATTERIES Date Device Carrier Aircraft Type," 2021. https://www.faa.gov/hazmat/resources/lithium_batteries/media/Battery_incident_chart.pdf.

[23] X. Feng *et al.*, "Investigating the thermal runaway mechanisms of lithium-ion batteries based on thermal analysis database," *Appl. Energy*, vol. 246, pp. 53–64, Jul. 2019, doi: 10.1016/J.APENERGY.2019.04.009.

[24] A. Bejan and S. Lorente, *Design with Constructal Theory*, vol. 22, no. 1 PART I. 2008.

[25] J. Yang, C. Hu, H. Wang, K. Yang, J. B. Liu, and H. Yan, "Review on the research of failure modes and mechanism for lead–acid batteries," *Int. J. Energy Res.*, vol. 41, no. 3, pp. 336–352, Mar. 2017, doi: https://doi.org/10.1002/er.3613.

[26] B. Hariprakash, S. A. Gaffoor, and A. K. Shukla, "Lead-acid batteries for partial-state-of-charge applications," *J. Power Sources*, vol. 191, no. 1, pp. 149–153, Jun. 2009, doi: 10.1016/j.jpowsour.2008.12.081.

[27] C. M. Diniş, G. N. Popa, and A. Iagər, "Study on sources of charging lead acid batteries," in *IOP Conference Series: Materials Science and Engineering*, Jun. 2015, vol. 85, no. 1, p. 012011, doi: 10.1088/1757-899X/85/1/012011.

[28] M. Fernández, J. Valenciano, F. Trinidad, and N. Muñoz, "The use of activated carbon and graphite for the development of lead-acid batteries for hybrid vehicle applications," *J. Power Sources*, vol. 195, no. 14, pp. 4458–4469, Jul. 2010, doi: 10.1016/j.jpowsour.2009.12.131.

[29] D. Linden and T. Reddy, *Handbook of Batteries*. McGraw-Hill Education, 2001.

[30] Y. Miao, P. Hynan, A. Von Jouanne, and A. Yokochi, "Current li-ion battery technologies in electric vehicles and opportunities for advancements," *Energies*, vol. 12, no. 6. Multidisciplinary Digital Publishing Institute, p. 1074, Mar. 20, 2019, doi: 10.3390/en12061074.

[31] T. M. Bandhauer, S. Garimella, and T. F. Fuller, "A Critical Review of Thermal Issues in Lithium-Ion Batteries," *J. Electrochem. Soc.*, 2011, doi: 10.1149/1.3515880.

[32] A. Väyrynen and J. Salminen, "Lithium ion battery production," *J. Chem. Thermodyn.*, vol. 46, pp. 80–85, Mar. 2012, doi: 10.1016/j.jct.2011.09.005.

[33] A. A. Pesaran, "Battery thermal models for hybrid vehicle simulations," 2002, doi: 10.1016/S0378-7753(02)00200-8.

[34] M. Doyle, “Modeling of Galvanostatic Charge and Discharge of the Lithium/Polymer/Insertion Cell,” *J. Electrochem. Soc.*, 1993, doi: 10.1149/1.2221597.

[35] Y. Chen, “Heat Transfer Phenomena in Lithium/Polymer-Electrolyte Batteries for Electric Vehicle Application,” *J. Electrochem. Soc.*, 1993, doi: 10.1149/1.2220724.

[36] Y. Chen, “Thermal Analysis of Lithium-Ion Batteries,” *J. Electrochem. Soc.*, 1996, doi: 10.1149/1.1837095.

[37] Y. Chen, “Three-Dimensional Thermal Modeling of Lithium-Polymer Batteries under Galvanostatic Discharge and Dynamic Power Profile,” *J. Electrochem. Soc.*, 1994, doi: 10.1149/1.2059263.

[38] V. Srinivasan and C. Y. Wang, “Analysis of Electrochemical and Thermal Behavior of Li-Ion Cells,” *J. Electrochem. Soc.*, 2003, doi: 10.1149/1.1526512.

[39] K. H. Kwon, C. B. Shin, T. H. Kang, and C. S. Kim, “A two-dimensional modeling of a lithium-polymer battery,” *J. Power Sources*, 2006, doi: 10.1016/j.jpowsour.2006.03.012.

[40] U. Seong Kim, J. Yi, C. B. Shin, T. Han, and S. Park, “Modeling the Dependence of the Discharge Behavior of a Lithium-Ion Battery on the Environmental Temperature,” *J. Electrochem. Soc.*, 2011, doi: 10.1149/1.3565179.

[41] A. Celik, H. Coban, S. Gocmen, M. A. Ezan, A. Gören, and A. Erek, “Passive thermal management of the lithium-ion battery unit for a solar racing car,” *Int. J. Energy Res.*, vol. 43, no. 8, pp. 3681–3691, 2019, doi: 10.1002/er.4521.

[42] R. Kizilel, A. Lateef, R. Sabbah, M. M. Farid, J. R. Selman, and S. Al-Hallaj, “Passive control of temperature excursion and uniformity in high-energy Li-ion battery packs at high current and ambient temperature,” *J. Power Sources*, 2008, doi: 10.1016/j.jpowsour.2008.04.050.

[43] N. Javani, I. Dincer, G. F. Naterer, and B. S. Yilbas, “Heat transfer and thermal management with PCMs in a Li-ion battery cell for electric vehicles,” *Int. J. Heat Mass Transf.*, 2014, doi: 10.1016/j.ijheatmasstransfer.2013.12.076.

[44] Z. Rao, Z. Qian, Y. Kuang, and Y. Li, “Thermal performance of liquid cooling based thermal management system for cylindrical lithium-ion battery module with variable contact surface,” *Appl. Therm. Eng.*, 2017, doi: 10.1016/j.applthermaleng.2017.06.059.

[45] L. H. Saw, Y. Ye, A. A. O. Tay, W. T. Chong, S. H. Kuan, and M. C. Yew,

"Computational fluid dynamic and thermal analysis of Lithium-ion battery pack with air cooling," *Appl. Energy*, 2016, doi: 10.1016/j.apenergy.2016.05.122.

[46] X. M. Xu and R. He, "Research on the heat dissipation performance of battery pack based on forced air cooling," *J. Power Sources*, 2013, doi: 10.1016/j.jpowsour.2013.03.004.

[47] A. A. Pesaran, "Battery thermal models for hybrid vehicle simulations," *J. Power Sources*, vol. 110, no. 2, pp. 377–382, Aug. 2002, doi: 10.1016/S0378-7753(02)00200-8.

[48] K. Chen, W. Wu, F. Yuan, L. Chen, and S. Wang, "Cooling efficiency improvement of air-cooled battery thermal management system through designing the flow pattern," *Energy*, vol. 167, pp. 781–790, Jan. 2019, doi: 10.1016/J.ENERGY.2018.11.011.

[49] T. Wang, K. J. Tseng, and J. Zhao, "Development of efficient air-cooling strategies for lithium-ion battery module based on empirical heat source model," *Appl. Therm. Eng.*, vol. 90, pp. 521–529, Nov. 2015, doi: 10.1016/J.APPLTHERMALENG.2015.07.033.

[50] S. Gungor, E. Cetkin, and S. Lorente, "Canopy-to-canopy liquid cooling for the thermal management of lithium-ion batteries, a constructal approach," *Int. J. Heat Mass Transf.*, vol. 182, p. 121918, Jan. 2022, doi: 10.1016/J.IJHEATMASSTRANSFER.2021.121918.

[51] M. S. Patil, J. H. Seo, S. Panchal, S. W. Jee, and M. Y. Lee, "Investigation on thermal performance of water-cooled Li-ion pouch cell and pack at high discharge rate with U-turn type microchannel cold plate," *Int. J. Heat Mass Transf.*, vol. 155, p. 119728, Jul. 2020, doi: 10.1016/J.IJHEATMASSTRANSFER.2020.119728.

[52] X. Xu, G. Tong, and R. Li, "Numerical study and optimizing on cold plate splitter for lithium battery thermal management system," *Appl. Therm. Eng.*, vol. 167, p. 114787, Feb. 2020, doi: 10.1016/J.APPLTHERMALENG.2019.114787.

[53] J. Lin, X. Liu, S. Li, C. Zhang, and S. Yang, "A review on recent progress, challenges and perspective of battery thermal management system," *Int. J. Heat Mass Transf.*, vol. 167, p. 120834, Mar. 2021, doi: 10.1016/J.IJHEATMASSTRANSFER.2020.120834.

[54] F. Chen *et al.*, "Air and PCM cooling for battery thermal management considering battery cycle life," *Appl. Therm. Eng.*, vol. 173, p. 115154, Jun. 2020, doi: 10.1016/J.APPLTHERMALENG.2020.115154.

[55] J. Chen *et al.*, “Effects of different phase change material thermal management strategies on the cooling performance of the power lithium ion batteries: A review,” *J. Power Sources*, vol. 442, p. 227228, Dec. 2019, doi: 10.1016/J.JPOWSOUR.2019.227228.

[56] B. Chidambaranathan, M. Vijayaram, V. Suriya, R. Sai Ganesh, and S. Soundarraj, “A review on thermal issues in Li-ion battery and recent advancements in battery thermal management system,” *Mater. Today Proc.*, vol. 33, pp. 116–128, Jan. 2020, doi: 10.1016/J.MATPR.2020.03.317.

[57] J. Xun, R. Liu, and K. Jiao, “Numerical and analytical modeling of lithium ion battery thermal behaviors with different cooling designs,” *J. Power Sources*, vol. 233, pp. 47–61, 2013, doi: https://doi.org/10.1016/j.jpowsour.2013.01.095.

[58] D. Chen, J. Jiang, G.-H. Kim, C. Yang, and A. Pesaran, “Comparison of different cooling methods for lithium ion battery cells,” *Appl. Therm. Eng.*, vol. 94, pp. 846–854, 2016, doi: https://doi.org/10.1016/j.applthermaleng.2015.10.015.

[59] S. A. Khateeb, M. M. Farid, J. R. Selman, and S. Al-Hallaj, “Design and simulation of a lithium-ion battery with a phase change material thermal management system for an electric scooter,” *J. Power Sources*, vol. 128, no. 2, pp. 292–307, 2004, doi: https://doi.org/10.1016/j.jpowsour.2003.09.070.

[60] L. Fan, J. M. Khodadadi, and A. A. Pesaran, “A parametric study on thermal management of an air-cooled lithium-ion battery module for plug-in hybrid electric vehicles,” *J. Power Sources*, vol. 238, pp. 301–312, 2013, doi: https://doi.org/10.1016/j.jpowsour.2013.03.050.

[61] Q. L. Yue, C. X. He, M. C. Wu, and T. S. Zhao, “Advances in thermal management systems for next-generation power batteries,” *Int. J. Heat Mass Transf.*, vol. 181, p. 121853, Dec. 2021, doi: 10.1016/J.IJHEATMASSTRANSFER.2021.121853.

[62] J. Jaguemont, N. Omar, P. Van den Bossche, and J. Mierlo, “Phase-change materials (PCM) for automotive applications: A review,” *Appl. Therm. Eng.*, vol. 132, pp. 308–320, 2018, doi: https://doi.org/10.1016/j.applthermaleng.2017.12.097.

[63] M. Al-Zareer, I. Dincer, and M. A. Rosen, “A review of novel thermal management systems for batteries,” *Int. J. Energy Res.*, vol. 42, no. 10, pp. 3182–3205, Aug. 2018, doi: 10.1002/ER.4095.

[64] T. Yuksel, S. Litster, V. Viswanathan, and J. J. Michalek, “Plug-in hybrid electric vehicle LiFePO4 battery life implications of thermal management, driving

conditions, and regional climate," *J. Power Sources*, vol. 338, pp. 49–64, 2017, doi: https://doi.org/10.1016/j.jpowsour.2016.10.104.

[65] H. Wang, F. He, and L. Ma, "Experimental and modeling study of controller-based thermal management of battery modules under dynamic loads," *Int. J. Heat Mass Transf.*, vol. 103, pp. 154–164, 2016, doi: https://doi.org/10.1016/j.ijheatmasstransfer.2016.07.041.

[66] X. Li, F. He, and L. Ma, "Thermal management of cylindrical batteries investigated using wind tunnel testing and computational fluid dynamics simulation," *J. Power Sources*, vol. 238, pp. 395–402, 2013, doi: https://doi.org/10.1016/j.jpowsour.2013.04.073.

[67] I. Voicu, H. Louahlia, H. Gualous, and R. Gallay, "Thermal management and forced air-cooling of supercapacitors stack," *Appl. Therm. Eng.*, vol. 85, pp. 89–99, 2015, doi: https://doi.org/10.1016/j.applthermaleng.2015.04.003.

[68] T. Wang, K. J. Tseng, and J. Zhao, "Development of efficient air-cooling strategies for lithium-ion battery module based on empirical heat source model," *Appl. Therm. Eng.*, vol. 90, pp. 521–529, 2015, doi: https://doi.org/10.1016/j.applthermaleng.2015.07.033.

[69] Z. Lu *et al.*, "Parametric study of forced air cooling strategy for lithium-ion battery pack with staggered arrangement," *Appl. Therm. Eng.*, vol. 136, pp. 28–40, 2018, doi: https://doi.org/10.1016/j.applthermaleng.2018.02.080.

[70] S. Park and D. Jung, "Battery cell arrangement and heat transfer fluid effects on the parasitic power consumption and the cell temperature distribution in a hybrid electric vehicle," *J. Power Sources*, vol. 227, pp. 191–198, 2013, doi: https://doi.org/10.1016/j.jpowsour.2012.11.039.

[71] K. Chen *et al.*, "Design of Parallel Air-Cooled Battery Thermal Management System through Numerical Study," *Energies* , vol. 10, no. 10. 2017, doi: 10.3390/en10101677.

[72] K. Chen, Y. Chen, Z. Li, F. Yuan, and S. Wang, "Design of the cell spacings of battery pack in parallel air-cooled battery thermal management system," *Int. J. Heat Mass Transf.*, vol. 127, pp. 393–401, Dec. 2018, doi: 10.1016/j.ijheatmasstransfer.2018.06.131.

[73] K. Chen, S. Wang, M. Song, and L. Chen, "Configuration optimization of battery pack in parallel air-cooled battery thermal management system using an optimization strategy," *Appl. Therm. Eng.*, vol. 123, pp. 177–186, Aug. 2017, doi:

10.1016/j.applthermaleng.2017.05.060.

[74] H. Park, “A design of air flow configuration for cooling lithium ion battery in hybrid electric vehicles,” *J. Power Sources*, 2013, doi: 10.1016/j.jpowsour.2013.03.102.

[75] X. M. Xu and R. He, “Research on the heat dissipation performance of battery pack based on forced air cooling,” *J. Power Sources*, vol. 240, pp. 33–41, Oct. 2013, doi: 10.1016/j.jpowsour.2013.03.004.

[76] H. Sun and R. Dixon, “Development of cooling strategy for an air cooled lithium-ion battery pack,” *J. Power Sources*, 2014, doi: 10.1016/j.jpowsour.2014.08.107.

[77] J. Xie, Z. Ge, M. Zang, and S. Wang, “Structural optimization of lithium-ion battery pack with forced air cooling system,” *Appl. Therm. Eng.*, vol. 126, pp. 583–593, Nov. 2017, doi: 10.1016/j.applthermaleng.2017.07.143.

[78] Y. Liu and J. Zhang, “Design a J-type air-based battery thermal management system through surrogate-based optimization,” *Appl. Energy*, vol. 252, p. 113426, Oct. 2019, doi: 10.1016/j.apenergy.2019.113426.

[79] E. Cetkin, “Constructal Microdevice Manifold Design with Uniform Flow Rate Distribution by Consideration of the Tree-Branching Rule of Leonardo da Vinci and Hess-Murray Rule,” *J. Heat Transfer*, 2017, doi: 10.1115/1.4036089.

[80] J. Lebæk, M. Bang, and S. K. Kær, “Flow and Pressure Distribution in Fuel Cell Manifolds,” *J. Fuel Cell Sci. Technol.*, vol. 7, no. 6, Aug. 2010, doi: 10.1115/1.4001319.

[81] S. Shahid and M. Agelin-Chaab, “Development and analysis of a technique to improve air-cooling and temperature uniformity in a battery pack for cylindrical batteries,” *Therm. Sci. Eng. Prog.*, vol. 5, pp. 351–363, Mar. 2018, doi: 10.1016/j.tsep.2018.01.003.

[82] J. Zhao, Z. Rao, Y. Huo, X. Liu, and Y. Li, “Thermal management of cylindrical power battery module for extending the life of new energy electric vehicles,” *Appl. Therm. Eng.*, vol. 85, pp. 33–43, Jun. 2015, doi: 10.1016/J.APPLTHERMALENG.2015.04.012.

[83] H. Wang, F. He, and L. Ma, “Experimental and modeling study of controller-based thermal management of battery modules under dynamic loads,” *Int. J. Heat Mass Transf.*, vol. 103, pp. 154–164, Dec. 2016, doi: 10.1016/J.IJHEATMASSTRANSFER.2016.07.041.

[84] J. E *et al.*, “Effects of the different air cooling strategies on cooling performance

of a lithium-ion battery module with baffle," *Appl. Therm. Eng.*, vol. 144, pp. 231–241, 2018, doi: https://doi.org/10.1016/j.applthermaleng.2018.08.064.

[85] T. Wang, K. J. Tseng, J. Zhao, and Z. Wei, "Thermal investigation of lithium-ion battery module with different cell arrangement structures and forced air-cooling strategies," *Appl. Energy*, 2014, doi: 10.1016/j.apenergy.2014.08.013.

[86] N. Yang, X. Zhang, G. Li, and D. Hua, "Assessment of the forced air-cooling performance for cylindrical lithium-ion battery packs: A comparative analysis between aligned and staggered cell arrangements," *Appl. Therm. Eng.*, vol. 80, pp. 55–65, 2015, doi: https://doi.org/10.1016/j.applthermaleng.2015.01.049.

[87] F. He, H. Wang, and L. Ma, "Experimental demonstration of active thermal control of a battery module consisting of multiple Li-ion cells," *Int. J. Heat Mass Transf.*, vol. 91, pp. 630–639, 2015, doi: https://doi.org/10.1016/j.ijheatmasstransfer.2015.07.069.

[88] R. Mahamud and C. Park, "Reciprocating air flow for Li-ion battery thermal management to improve temperature uniformity," *J. Power Sources*, vol. 196, no. 13, pp. 5685–5696, 2011, doi: https://doi.org/10.1016/j.jpowsour.2011.02.076.

[89] T. Özdemir, A. Amini, Ö. Ekici, and M. Köksal, "Experimental Assessment of the Lumped Lithium Ion Battery Model at Different Operating Conditions," *https://doi.org/10.1080/01457632.2021.1874666*, 2021, doi: 10.1080/01457632.2021.1874666.

[90] J. Jaguemont and J. Van Mierlo, "A comprehensive review of future thermal management systems for battery-electrified vehicles," *J. Energy Storage*, vol. 31, p. 101551, 2020, doi: https://doi.org/10.1016/j.est.2020.101551.

[91] L. Zhu, R. F. Boehm, Y. Wang, C. Halford, and Y. Sun, "Water immersion cooling of PV cells in a high concentration system," *Sol. Energy Mater. Sol. Cells*, vol. 95, no. 2, pp. 538–545, 2011, doi: https://doi.org/10.1016/j.solmat.2010.08.037.

[92] S. Yang, C. Ling, Y. Fan, Y. Yang, X. Tan, and H. Dong, "A review of lithium-ion battery thermal management system strategies and the evaluate criteria," *International Journal of Electrochemical Science*. 2019, doi: 10.20964/2019.07.06.

[93] A. M. Sefidan, A. Sojoudi, and S. C. Saha, "Nanofluid-based cooling of cylindrical lithium-ion battery packs employing forced air flow," *Int. J. Therm. Sci.*, vol. 117, pp. 44–58, 2017, doi: https://doi.org/10.1016/j.ijthermalsci.2017.03.006.

[94] R. W. van Gils, D. Danilov, P. H. L. Notten, M. F. M. Speetjens, and H. Nijmeijer,

"Battery thermal management by boiling heat-transfer," *Energy Convers. Manag.*, vol. 79, pp. 9–17, 2014, doi: https://doi.org/10.1016/j.enconman.2013.12.006.

[95] T. Endo, A. Nukada, and S. Matsuoka, "TSUBAME-KFC: A modern liquid submersion cooling prototype towards exascale becoming the greenest supercomputer in the world," 2014, doi: 10.1109/PADSW.2014.7097829.

[96] W. Wu, S. Wang, W. Wu, K. Chen, S. Hong, and Y. Lai, "A critical review of battery thermal performance and liquid based battery thermal management," *Energy Convers. Manag.*, vol. 182, pp. 262–281, Feb. 2019, doi: 10.1016/J.ENCONMAN.2018.12.051.

[97] W. A. Hermann, "Liquid cooling manifold with multi-function thermal interface," 2010.

[98] A. Faas and E. Clough, "Battery module with integrated thermal management system," 2012.

[99] C. Zhao, W. Cao, T. Dong, and F. Jiang, "Thermal behavior study of discharging/charging cylindrical lithium-ion battery module cooled by channeled liquid flow," *Int. J. Heat Mass Transf.*, vol. 120, pp. 751–762, 2018, doi: https://doi.org/10.1016/j.ijheatmasstransfer.2017.12.083.

[100] J. W. Xu, T. S. Zhou, and X. H. Xu, "Experimental investigation on a novel liquid cooling device for a prismatic Li-ion battery module operating at high ambient temperature," *Sci. China Technol. Sci. 2020 6310*, vol. 63, no. 10, pp. 2147–2153, Jun. 2020, doi: 10.1007/S11431-020-1605-5.

[101] S. Panchal, I. Dincer, M. Agelin-Chaab, R. Fraser, and M. Fowler, "Experimental temperature distributions in a prismatic lithium-ion battery at varying conditions," *Int. Commun. Heat Mass Transf.*, vol. 71, pp. 35–43, Feb. 2016, doi: 10.1016/J.ICHEATMASSTRANSFER.2015.12.004.

[102] S. Basu, K. S. Hariharan, S. M. Kolake, T. Song, D. K. Sohn, and T. Yeo, "Coupled electrochemical thermal modelling of a novel Li-ion battery pack thermal management system," *Appl. Energy*, vol. 181, pp. 1–13, 2016, doi: https://doi.org/10.1016/j.apenergy.2016.08.049.

[103] J. Zhao, Z. Rao, and Y. Li, "Thermal performance of mini-channel liquid cooled cylinder based battery thermal management for cylindrical lithium-ion power battery," *Energy Convers. Manag.*, vol. 103, pp. 157–165, 2015, doi: https://doi.org/10.1016/j.enconman.2015.06.056.

[104] M. Al-Zareer, I. Dincer, and M. A. Rosen, "A review of novel thermal management

systems for batteries," *International Journal of Energy Research*. 2018, doi: 10.1002/er.4095.

[105] S. Al Hallaj and J. R. Selman, "A Novel Thermal Management System for Electric Vehicle Batteries Using Phase-Change Material," *J. Electrochem. Soc.*, 2000, doi: 10.1149/1.1393888.

[106] Z. Wang, H. Zhang, and X. Xia, "Experimental investigation on the thermal behavior of cylindrical battery with composite paraffin and fin structure," *Int. J. Heat Mass Transf.*, vol. 109, pp. 958–970, Jun. 2017, doi: 10.1016/J.IJHEATMASSTRANSFER.2017.02.057.

[107] C. Guo and W. Zhang, "Numerical simulation and parametric study on new type of high temperature latent heat thermal energy storage system," *Energy Convers. Manag.*, vol. 49, no. 5, pp. 919–927, 2008, doi: https://doi.org/10.1016/j.enconman.2007.10.025.

[108] A. Lazrak, J.-F. Fourmigué, and J.-F. Robin, "An innovative practical battery thermal management system based on phase change materials: Numerical and experimental investigations," *Appl. Therm. Eng.*, vol. 128, pp. 20–32, 2018, doi: https://doi.org/10.1016/j.applthermaleng.2017.08.172.

[109] Z. Wang, H. Zhang, and X. Xia, "Experimental investigation on the thermal behavior of cylindrical battery with composite paraffin and fin structure," *Int. J. Heat Mass Transf.*, vol. 109, pp. 958–970, 2017, doi: https://doi.org/10.1016/j.ijheatmasstransfer.2017.02.057.

[110] R. Sabbah, R. Kizilel, J. R. Selman, and S. Al-Hallaj, "Active (air-cooled) vs. passive (phase change material) thermal management of high power lithium-ion packs: Limitation of temperature rise and uniformity of temperature distribution," *J. Power Sources*, 2008, doi: 10.1016/j.jpowsour.2008.03.082.

[111] S. A. Khateeb, S. Amiruddin, M. Farid, J. R. Selman, and S. Al-Hallaj, "Thermal management of Li-ion battery with phase change material for electric scooters: experimental validation," *J. Power Sources*, vol. 142, no. 1, pp. 345–353, 2005, doi: https://doi.org/10.1016/j.jpowsour.2004.09.033.

[112] F. Samimi, A. Babapoor, M. Azizi, and G. Karimi, "Thermal management analysis of a Li-ion battery cell using phase change material loaded with carbon fibers," *Energy*, vol. 96, pp. 355–371, 2016, doi: https://doi.org/10.1016/j.energy.2015.12.064.

[113] H. Sun and R. Dixon, "Development of cooling strategy for an air cooled lithium-

ion battery pack," *J. Power Sources*, vol. 272, pp. 404–414, Dec. 2014, doi: 10.1016/j.jpowsour.2014.08.107.

[114] A. Bejan, *Convection Heat Transfer*, 4th ed. Wiley, 2013.

[115] J. W. Mitchell, R. W. Fox, and A. T. McDonald, "Fox and McDonald's introduction to fluid mechanics.," p. 6, Accessed: Nov. 07, 2021. [Online]. Available: https://www.wiley.com/en-us/Fox+and+McDonald%27s+Introduction+to+Fluid+Mechanics%2C+10th+Edition-p-9781119603764.

[116] *ANSYS Fluent Theory Guide 18.2*. .

[117] H. Gu, "Mathematical Analysis of a Zn/NiOOH Cell," *J. Electrochem. Soc.*, 1983, doi: 10.1149/1.2120009.

[118] S. Zhang, "A Hydrogel Based Thermal Management System for Lithium-ion Batteries," 2014.

[119] Y. Xie, S. Shi, J. Tang, H. Wu, and J. Yu, "Experimental and analytical study on heat generation characteristics of a lithium-ion power battery," *Int. J. Heat Mass Transf.*, vol. 122, pp. 884–894, Jul. 2018, doi: 10.1016/J.IJHEATMASSTRANSFER.2018.02.038.

[120] S. J. Bazinski and X. Wang, "Predicting heat generation in a lithium-ion pouch cell through thermography and the lumped capacitance model," *J. Power Sources*, vol. 305, pp. 97–105, Feb. 2016, doi: 10.1016/J.JPOWSOUR.2015.11.083.

[121] C. Lin, S. Xu, and J. Liu, "Measurement of heat generation in a 40 Ah LiFePO4 prismatic battery using accelerating rate calorimetry," *Int. J. Hydrogen Energy*, vol. 43, no. 17, pp. 8375–8384, Apr. 2018, doi: 10.1016/J.IJHYDENE.2018.03.057.

[122] L. Sheng, L. Su, H. Zhang, Y. Fang, H. Xu, and W. Ye, "An improved calorimetric method for characterizations of the specific heat and the heat generation rate in a prismatic lithium ion battery cell," *Energy Convers. Manag.*, vol. 180, pp. 724–732, Jan. 2019, doi: 10.1016/J.ENCONMAN.2018.11.030.

[123] V. Srinivasan, "Batteries for Vehicular Applications," *AIP Conf. Proc.*, vol. 1044, no. 1, p. 283, Sep. 2008, doi: 10.1063/1.2993726.